

# **Numerical study of Aeroacoustic sources generated from the wake behind the car**

Master's thesis in Applied Mechanics

**BARLEV RAYMOND NAGAWKAR**



MASTER'S THESIS 2016:70

**Numerical study of Aeroacoustic sources  
generated from the wake behind the car**

BARLEV RAYMOND NAGAWKAR



**CHALMERS**  
UNIVERSITY OF TECHNOLOGY

Department of Applied Mechanics  
*Division of Fluid Mechanics*  
CHALMERS UNIVERSITY OF TECHNOLOGY  
Gothenburg, Sweden 2016

Numerical study of Aeroacoustic sources generated from the wake behind the car  
BARLEV RAYMOND NAGAWKAR

© BARLEV RAYMOND NAGAWKAR, 2016.

Supervisor: Prof. Sinisa Krajnovic and Dr. Huadong Yao, Fluid Dynamics  
Examiner: Prof. Sinisa Krajnovic, Fluid Dynamics

Master's Thesis 2016:70  
Division of Fluid Dynamics  
Department of Applied Mechanics  
Chalmers University of Technology  
SE-412 96 Gothenburg  
Telephone +46 31 772 1000

Cover: Streamlines of average velocity for selected planes on and in the wake of the geometry.

Printed by [Chalmers Reproservice]  
Gothenburg, Sweden 2016

Numerical study of Aeroacoustic sources generated from the wake behind the car  
BARLEV RAYMOND NAGAWKAR  
Division of Department of Applied Mechanics  
Chalmers University of Technology

## **Abstract**

Due to new legislative and consumer demands Europe's major vehicle manufactures (Original Equipment Manufacturer, OEMs) are forced to make big investments in the area of aeroacoustics. To measure a small noise contribution in wind tunnels is a challenge. Do to uncertainties of physical testing, the importance of using numerical methods for aeroacoustics has gone up.

In this thesis an aeroacoustics study is performed on generic bodies with a focus on the wake. Three types of Ahmed bodies are used namely, the slant or fast back, the square or bus back and the notch or sedan back. The geometries being different in the rear will generate different wake structures and difference in noise levels obtained from these are analysed.

An hybrid computational aeroacoustic method is adopted where first Large Eddy Simulations (LES) are done using AVL Fire to simulate the flow field. The sound propagation is then solved by using the Curle acoustic analogy.

Keywords: Aeroacoustics, Curle, Large Eddy Simulations, Ahmed body, CFD, CAA



# Contents

<b>Nomenclature</b>	<b>ix</b>
<b>List of Figures</b>	<b>xi</b>
<b>List of Tables</b>	<b>xiii</b>
<b>1 Introduction</b>	<b>1</b>
1.1 Background . . . . .	1
1.2 Objective . . . . .	2
1.3 Delimitation . . . . .	2
<b>2 Theory</b>	<b>3</b>
2.1 Fluid Mechanics . . . . .	3
2.1.1 Governing equations . . . . .	3
2.1.1.1 The continuity equation . . . . .	3
2.1.1.2 The momentum equation . . . . .	3
2.1.2 Important dimensionless quantities . . . . .	4
2.1.2.1 Reynolds number . . . . .	4
2.1.2.2 Mach number . . . . .	4
2.1.2.3 Strouhal number . . . . .	4
2.2 Turbulence modeling . . . . .	5
2.2.1 Large Eddy Simulation (LES) . . . . .	5
2.2.1.1 Filtering . . . . .	5
2.2.1.2 Sub-grid model . . . . .	6
2.3 Aeroacoustics . . . . .	7
2.3.1 Classical Wave equation . . . . .	7
2.3.2 Sources of sound . . . . .	8
2.3.2.1 Monopole . . . . .	8
2.3.2.2 Dipole . . . . .	8
2.3.2.3 Quadrupole . . . . .	8
2.3.3 Computational Aeroacoustics (CAA) . . . . .	9
2.3.3.1 Lighthill's acoustic analogy . . . . .	9
2.3.3.2 Curle Method- special case of FW-H . . . . .	11
<b>3 Methods</b>	<b>13</b>
3.1 Workflow . . . . .	13
3.2 Geometry and Domain . . . . .	13

3.2.1	Geometry . . . . .	13
3.2.2	Computational Domain . . . . .	14
3.3	Mesh . . . . .	15
3.3.1	Mesh requirements . . . . .	15
3.3.1.1	For LES . . . . .	15
3.3.1.2	For aeroacoustics . . . . .	15
3.3.2	Mesh details for geometries . . . . .	15
3.4	Numerical setup for CFD . . . . .	17
3.4.1	Transient . . . . .	17
3.4.2	Incompressibility . . . . .	17
3.4.3	Boundary conditions . . . . .	18
3.4.4	Data for Aeroacoustics . . . . .	18
3.5	Acoustics solver . . . . .	18
3.6	Postprocessing . . . . .	19
<b>4</b>	<b>Results</b>	<b>21</b>
4.1	Computational Fluid Dynamics . . . . .	21
4.1.1	Slant-back . . . . .	21
4.1.2	Notch-back . . . . .	24
4.1.3	Square-back . . . . .	27
4.2	Aeroacoustics . . . . .	29
4.2.1	Sound Pressure Level (SPL) . . . . .	29
4.2.2	Overall Sound Pressure Level (OASPL) . . . . .	30
<b>5</b>	<b>Discussion</b>	<b>33</b>
5.1	Comparison of flow . . . . .	33
5.2	Comparison of Noise . . . . .	34
5.3	Identifying sources . . . . .	34
5.3.1	Slant-back . . . . .	34
5.3.2	Notch-back . . . . .	37
<b>6</b>	<b>Conclusion</b>	<b>41</b>
	<b>Bibliography</b>	<b>43</b>
<b>A</b>	<b>Appendix</b>	<b>I</b>

# Nomenclature

## Latin symbols

$a, c_o$	Speed of sound
$C_p$	Heat capacity at constant pressure
$C_v$	Heat capacity at constant volume
$C_s$	Smagorinsky constant
$f$	Frequency
$f_i$	Body force
$F_i$	Unsteady external force
$f_\mu$	Damping function
$G_B$	Filter function
$H$	Height of vehicle
$L$	Characteristic length
$l^+$	Spanwise resolution
$m$	Mass rate
$Ma, M$	Mach number
$n$	Wall normal distance
$n^+$	Wall normal resolution
$n_i$	Normal vector
$P$	Pressure
$p'$	Pressure perturbation/ fluctuation
$p'_{rms}$	Root mean square of pressure fluctuation
$p'_{ref}$	Reference sound pressure
$r$	Distance between observer and source
$R$	Speific gas constant
$Re$	Reynolds number
$S_{ij}$	Strain rate tensor
$\bar{s}_{ij}$	Averaged strain rate tensor
$s^+$	Streamwise resolution
$t$	Time
$T$	Temperature
$T_{ij}$	Lighthill tensor
$\Delta t$	Time step size

$u$	Characteristic velocity scale
$u_*$	Friction velocity
$V$	Flow velocity
$V_\infty$	Free-stream velocity
$v_i$	Velocity in $i$ direction
$\Delta V_{IJK}$	Local cell size
$x_i$	Coordinate in ' $i$ ' direction
$x_2^+$	dimensionless wall number
$\Delta x$	Smallest cell size
$\mathbf{x}$	Position of observer
$\mathbf{y}$	Position of source

### Greek symbols

$\gamma$	Specific heat ratio
$\delta_{ij}$	Kronecker's delta
$\Delta$	Filter width
$\lambda$	Wavelength
$\mu$	Dynamic viscosity
$\nu$	Kinematic viscosity
$\nu_{SGS}$	SGS turbulent viscosity
$\rho$	Density
$\rho'$	Density fluctuations
$\tau_{ij}$	Shear stress tensor
$\tau_r$	Retarded time
$\tau_w$	Wall shear stress

### Abbreviation

CAA	Computational Aeroacoustics
CFD	Computational Fluid Dynamics
CFL	Courant–Friedrichs–Lewy
DES	Detached Eddy Simulation
DNS	Direct Numerical Simulation
LES	Large Eddy Simulation
OASPL	Overall Sound Pressure Level
OEM	Original Equipment Manufacturer
RANS	Reynolds Averaged Navier-Stokes
SGS	Sub-Grid Scales
SPL	Sound Pressure Level
URANS	Unsteady Reynolds Averaged Navier-Stokes

### Miscellaneous

$\square^2$	d'Alembert operator
-------------	---------------------

# List of Figures

3.1	Slant-back . . . . .	14
3.2	Notch-back . . . . .	14
3.3	Square-back . . . . .	14
3.4	Domain . . . . .	14
3.5	Temperature plots, Gauss Seidel . . . . .	16
3.6	Mic Positions . . . . .	19
3.7	Monitor points for notch back . . . . .	20
4.1	View from top . . . . .	21
4.2	Side view . . . . .	22
4.3	View from front/back . . . . .	23
4.4	Instantaneous pressure . . . . .	23
4.5	Top view . . . . .	24
4.6	Side view . . . . .	25
4.7	Front/back view . . . . .	26
4.8	Instantaneous pressure . . . . .	26
4.9	Top view . . . . .	27
4.10	Side view . . . . .	27
4.11	Front/back view . . . . .	27
4.12	Instantaneous pressure . . . . .	28
4.13	SPL for selected mic positions . . . . .	29
4.14	OASPL around the car . . . . .	30
4.15	OASPL front to back . . . . .	31
4.16	OASPL side to side in wake . . . . .	31
5.1	Pressure in spectra on top of body . . . . .	35
5.2	Far field noise, wake . . . . .	35
5.3	Near field on top of slant region . . . . .	36
5.4	Near field in wake . . . . .	36
5.5	Pressure in spectra . . . . .	37
5.6	Pressure in spectra . . . . .	37
5.7	Far field noise, top . . . . .	38
5.8	Far field noise, wake . . . . .	38
5.9	Pressure in spectra on deck . . . . .	39
5.10	Pressure in spectra . . . . .	39



# List of Tables

3.1	Mesh details . . . . .	17
3.2	Boundary conditions . . . . .	18



# 1

## Introduction

Aero-acoustics, simply put, is the study of air flow induced noise. The need to reduce noise from jet engines lead to the development of the field in the 1950s. With the increase in computation power various numerical methods have been developed to solve this problem in various engineering applications. This thesis is a study of the noise induced by external air flow around different car shapes with a focus on the wake.

### 1.1 Background

Stapleford and Carr [1] divided the flow induced noise for ground vehicles in three categories

- Unpitched noise caused by air rushing past the exterior of the car
- Monotone noise caused by sharp edges and gaps on the exterior or the car
- Flow excitation of openings in the vehicles such as side windows and sun-roof which influence the compartment noise level.

The first category is also called the air rush noise or wind noise and is the focus of the thesis. This sound is expected to dominate other sources at speeds above  $100 - 160\text{km/h}$ .

In 1964 Thomson [3] conducted road tests to investigate whether aerodynamic shape noise is the source that contributes to most wind noise. He found the most critical region were the foremost part of the side windows, the A pillar sealing followed by the C pillar region close to the belt-line and the front door region close to the driver or passenger. The two part study was done by Stapleford and Carr [1, 2] to associate different flow regimes with aerodynamic noise level for generic objects and production vehicles. They found that the aerodynamic noise levels were highly associated with different forms of flow separation, particularly spiral vortex flows downstream of the A pillar.

Due to new legislative and consumer demands Europe's major vehicle manufacturers (OEMs) are forced to make big investments in the area of aeroacoustics. To measure a small noise contribution in wind tunnel is a challenge. Do to uncertainties of physical testing, the importance of using numerical methods for aeroacoustics has gone up.

Numerical methods have been adopted to investigate the noise for generic or realistic mirrors. Rung et al. [4] conducted flow and noise generation study for generic side mirrors in comparison of URANS and DES. Posson and Perot [5] took

the geometry complexity a step further by mounting a production mirror on top of a plate and exposing it to freestream velocity of 40m/s. Duncan et al. [6] performed simulations on a Ahmed body and did a spectral analysis to visually identify noise sources for restricted frequency bands. There seems to be limited work in the field with focus on the wake of the vehicle and this thesis is the basis for such a study.

## 1.2 Objective

The main objective of the thesis is to establish a methodology to solve the aeroacoustics problem for external air flow around a car. Once the method established the goal is to apply it to three generic car geometries with different shapes of the rear. The three shapes are the the slant-back, square-back and notch-back. Due to the difference in the shapes the turbulent structures in then wake would be different. Theses would be computed and analysed with CFD and the resulting sound propagation due to these different wake structures would be analysed by performing a Computational aeroacoustic calculation.

## 1.3 Delimitation

The delimitation's of the study are as follows:

- Generic car body: the geometry used generic car shapes. The reason for using simplified geometries is to establish a methodology first. This is to reduce to computational cost while giving essential understanding the flow, such as the wake.
- Low Reynolds number flow: Large Eddy Simulations (LES) were done and a Reynolds number of 10000 was chosen to keep the computational cost low. This implies a low velocity for the chosen geometry.

Typically the noise generated by the air rush dominates above  $100km/h$  for road vehicles [9]. For cars, that is a Reynolds number higher than  $2 \cdot 10^6$ . This would mean the noise calculation would not be in the audible range of humans.

# 2

## Theory

In this section a summary of the theory relevant to the thesis is described. This involves certain topics from fluid mechanics, computational fluid mechanics (CFD), turbulence modeling, aeroacoustics and computational aeroacoustics (CAA).

### 2.1 Fluid Mechanics

#### 2.1.1 Governing equations

##### 2.1.1.1 The continuity equation

The continuity equation is the balance equation for mass and is given as

$$\frac{d\rho}{dt} + \frac{\partial \rho v_i}{\partial x_i} = 0 \quad (2.1)$$

For incompressible flow, the density is constant. Therefore eq 2.1 reads

$$\frac{\partial v_i}{\partial x_i} = 0 \quad (2.2)$$

##### 2.1.1.2 The momentum equation

This is called the Navier-Stokes equation and is a transport equation for momentum. It is given by

$$\rho \frac{dv_i}{dt} = -\frac{\partial P}{\partial x_i} + \frac{\partial \tau_{ji}}{\partial x_i} + \rho f_i \quad (2.3)$$

Alternatively,

$$\frac{\partial \rho v_i}{\partial t} + \frac{\partial \rho v_i v_j}{\partial x_j} = -\frac{\partial P}{\partial x_i} + \frac{\partial \tau_{ji}}{\partial x_i} \quad (2.4)$$

Here,

$$\tau_{ji} = 2\mu S_{ij} - \frac{2}{3}\mu S_{kk}\delta_{ij} \quad (2.5)$$

Where  $\mu$  is dynamics viscosity and

$$S_{ij} = \frac{1}{2} \left( \frac{\partial v_i}{\partial x_j} + \frac{\partial v_j}{\partial x_i} \right) \quad (2.6)$$

For constant  $\mu$  incompressible flow, equation 2.3 can be written as

$$\rho \frac{dv_i}{dt} = -\frac{\partial P}{\partial x_i} + \mu \frac{\partial^2 v_i}{\partial x_i \partial x_j} + \rho f_i \quad (2.7)$$

Alternatively neglecting body force term and expressing the term on the left in its non conservative form

$$\frac{\partial v_i}{\partial t} + v_j \frac{\partial v_i}{\partial x_j} = -\frac{1}{\rho} \frac{\partial P}{\partial x_i} + \nu \frac{\partial^2 v_i}{\partial x_i \partial x_j} \quad (2.8)$$

Where  $\nu$  is the kinematic viscosity

## 2.1.2 Important dimensionless quantities

### 2.1.2.1 Reynolds number

The Reynolds number is defined as the ratio of inertial forces to viscous forces. It is used to describe the flow patterns for a given fluid flow situation, by indicating whether the flow is laminar or turbulent. It is expressed as,

$$Re = \frac{V_\infty L}{\nu} \quad (2.9)$$

Where  $V_\infty$  is the flow velocity,  $L$  is the characteristic length and  $\nu$  is the kinematic viscosity. The Reynolds number is used for scaling a fluid dynamics problem and determining similitude between two different cases of flow.

### 2.1.2.2 Mach number

This is the ratio of local velocity of flow to the speed of sound. It is given by

$$Ma = \frac{V}{a} \quad (2.10)$$

The Mach number is used to determine the approximation of incompressibility. For  $M < 0.3$ , air is assumed to be incompressible. This is because compressibility has negligible effects on flow [7].

### 2.1.2.3 Strouhal number

This represents the ratio of the inertial forces due to unsteadiness of the flow or local acceleration to the inertial forces due to change in velocity from one point to the other in the flow field. It is important while analysing unsteady, oscillating flow problems. It is formulated as

$$St = \frac{fL}{V_\infty} \quad (2.11)$$

Where  $f$  is the oscillating frequency,  $L$  is the characteristic length and  $V_\infty$  is the flow velocity. Dominant Strouhal numbers of bluff body wakes are usually within a range of 0.2 for circular cylinders and 0.26 for short D-shaped bodies, Leder 1992 [8]. This is useful in order to estimate tonal peaks caused by vortex shedding.

## 2.2 Turbulence modeling

In turbulent flow, velocity and pressure are unsteady and include all turbulent motion, often called eddies. The spatial scales of these eddies vary in magnitude from large eddies which are proportional to the size of the largest physical length scale to smallest eddies where dissipation takes place. Dissipation is where kinetic energy is transformed to internal energy.

Turbulent flow problems are solved numerically in two ways; Direct Numerical Simulation (DNS) and Turbulence Models. DNS is the most accurate method available as it gives the exact solution of the flow field in time and space. However this method is only feasible for low Reynolds number. Higher the Reynolds number, finer the grid must be to resolve the Kolmogorov scales as the smallest length and time scales decrease with  $Re^{-3/4}$  and  $Re^{-3/4}$  respectively. This makes it computationally expensive to solve the Navier-Stokes equation for high Reynolds numbers.

To solve the Navier-Stokes equation with a reasonable computational cost, turbulence models are used. They are in essence an approximation of the Navier-Stokes equation. These models are Large Eddy Simulation (LES), Reynolds Averaged Navier-Stokes (RANS) and hybrid RANS/LES Models. In this thesis only LES was performed and hence on this shall be described here [10].

### 2.2.1 Large Eddy Simulation (LES)

Here the small eddies are modeled and only the large eddies are resolved. Small eddies refer to the eddies with scales smaller than the grid size (computational cell size) and the eddies larger than the grid size are resolved by the filtered Navier-Stokes equation. In LES instead of time averaging, volume averaging (filtering) is done. The filtered variables are then a function of both space and time. The LES equation reads

$$\frac{\partial \bar{v}_i}{\partial t} + \frac{\partial \bar{v}_i \bar{v}_j}{\partial x_j} = -\frac{1}{\rho} \frac{\partial \bar{p}}{\partial x_i} + \nu \frac{\partial^2 \bar{v}_i}{\partial x_i \partial x_j} - \frac{\partial \tau_{ij}}{\partial x_j} \quad (2.12)$$

The first term is kept because the large, time dependant fluctuations are part of  $v_i$  and  $p$  and are not modeled. The last term includes the Reynolds stress of all the small eddies and are called sub-grid stresses (SGS). This term is given by

$$\tau_{ij} = \bar{v}_i \bar{v}_j - \bar{v}_i \bar{v}_j \quad (2.13)$$

#### 2.2.1.1 Filtering

The separation of resolved large scales and modeled small scales is done by filtering. It is formally defines as

$$\bar{v}(x) = \int_{-\infty}^{\infty} G_B(r) v(x-r) dr \quad (2.14)$$

$$G_B(r) = \begin{cases} 1/\Delta, & r < \Delta/2 \\ 0, & r > \Delta \end{cases}$$

This equation is a representation in 1D where  $G_B$  is the filter function and  $\Delta$  is the filter width. The spacial filter can also be expressed as

$$\bar{f}(x_i) = \int_{\Omega} f(x'_i)G(x_i, x'_i)dx'_i \quad (2.15)$$

where  $f$  is the quantity to be filtered.

In finite volume method the filtering is the same as the discretization. So the filter width is taken as the local grid size [14], given as

$$\Delta = (\Delta V_{IJK})^{1/3} \quad (2.16)$$

### 2.2.1.2 Sub-grid model

A sub-grid model is needed to model the eddies with scales smaller than the grid size. This is done by modeling it with the turbulent SGS viscosity and is called the Smoagorinsky Model.

$$\tau_{ij} - \frac{1}{3}\delta_{ij}\tau_{kk} = -\nu_{SGS} \left( \frac{\partial \bar{v}_i}{\partial x_j} + \frac{\partial \bar{v}_j}{\partial x_i} \right) = -2\nu_{SGS}|\bar{s}_{ij}| \quad (2.17)$$

So equation 2.12 can be expressed as

$$\frac{\partial \bar{v}_i}{\partial t} + \frac{\partial \bar{v}_i \bar{v}_j}{\partial x_j} = -\frac{1}{\rho} \frac{\partial \bar{p}}{\partial x_i} + \frac{\partial}{\partial x_j} \left( (\nu + \nu_{SGS}) \frac{\partial v_i}{\partial x_j} \right) \quad (2.18)$$

The turbulent SGS viscosity is give by

$$\nu_{SGS} = (C_S \Delta)^2 \sqrt{2\bar{s}_{ij}2\bar{s}_{ij}} \quad (2.19)$$

Where  $C_S$  is called the Smagorinsky constant, although its value is flow dependant and varies from the range 0.065 to 0.25, and  $\Delta$  is the filter width. The SGS viscosity near the wall gets really high near the wall because the gradient of velocity is high. However the SGS turbulent fluctuations near the wall goes to zero, therefore so should the SGS viscosity. This is ensured by using a damping function  $f_\mu$  which is given by

$$f_\mu = 1 - \exp(-x_2^+/26) \quad (2.20)$$

## 2.3 Aeroacoustics

Sound can be defined as a pressure perturbation  $p'$  which propagates as a wave and is detectable to the human ear. For harmonic pressure fluctuations the range of frequency of the human ear is between 20Hz and 20kHz. The human ear has a logarithmic sensitivity, hence we use a decibel scale to measure sound level. The Sound Pressure Level (SPL) is given by

$$SPL = 20 \cdot \log_{10} \left( \frac{p'_{rms}}{p_{ref}} \right) = 10 \cdot \log_{10} \left( \frac{p'_{rms}}{p_{ref}} \right)^2 \quad (2.21)$$

where  $p'_{rms}$  is the root mean square of the acoustics pressure fluctuation  $p'$ , and  $p_{ref} = 2 \cdot 10^{-5} Pa$  in air.

Speed of sound is defined as isentropic change in pressure with change in density

$$c_o = \sqrt{\left( \frac{\partial p}{\partial \rho} \right)_s} = \sqrt{\gamma RT} \quad (2.22)$$

where  $\gamma = C_p/C_v$  is the specific heat ratio, R is the specific gas constant. The speed of sound in air is  $346.65m/s$  at  $298.15K$ .

### 2.3.1 Classical Wave equation

It was Laplace who suggest a model that gave the first correct derivation of the classical wave equation. In the 19th century Kirchhoff, Helmholtz and Rayleigh laid ground for classical theory of sound in fluids [11]. The classical wave equation is valid in an isentropic, homogeneous fluid at rest. The equation is given as

$$\frac{1}{c_o^2} \frac{\partial^2 p}{\partial t^2} - \frac{\partial^2 p}{\partial x_i^2} = \square^2 p = 0 \quad (2.23)$$

or,

$$\frac{1}{c_o^2} \frac{\partial^2 \rho}{\partial t^2} - \frac{\partial^2 \rho}{\partial x_i^2} = \square^2 \rho = 0 \quad (2.24)$$

where  $\square^2$  is called the d'Alembert operator or the wave operator and  $c_o$  is the isentropic speed of sound. In regions of turbulent flow,  $\square^2 p \neq 0$

This equation is derived from the continuity and momentum equations of flow. Apart from the above mentioned assumption the derivation neglects the source terms from the equations. Theses are the unsteady mass injections and unsteady external forces from respective governing flow equations. This means that the wave equation has no source term and doesn't account for sound generation by unsteady fluid flow. This was not a large issue a hundred years ago but became an important problem in the 1950's with the development of the commercial jet engine. The need to reduce the noise led to understand the underlying mechanisms. It was Sir James Lighthill who published the a paper in 1952 on aerodynamics noise which marked the birth of the new field of research, aeroacoustics.

### 2.3.2 Sources of sound

Typically there are three types of sound sources namely, monopole, dipole and quadrupole.

#### 2.3.2.1 Monopole

This is the strongest type of acoustic sources and is defined as,

$$\square^2 \rho = \frac{\partial m}{\partial t} \quad (2.25)$$

where m is mass rate and the source mechanism is mass injection which acts as a pulsating sphere where sound is radiated uniformly in all directions. Hirschberg and Rienstra [12] describe this a person jumping on a boat providing unsteady supply of volume generating a monopole wave pattern around the boat. The pressure fluctuations are dependant on velocity and will scale as

$$p'_m \propto u^2 \quad (2.26)$$

where u is the characteristic velocity scale of the source fluctuation [13].

#### 2.3.2.2 Dipole

This source term is given as

$$\square^2 \rho = -\frac{\partial F_i}{\partial x_i} \quad (2.27)$$

where F is the unsteady external force in the fluid flow. The dipole source consists of two monopole sources alternatively expanding and contracting. Hirschberg and Rienstra [12] describe this as two people playing with a ball tossing it back and forth making the boat oscillate creating a dipole wave field around it. This is proportional to velocity and Mach number [13] as

$$p'_d \propto u^2 M \quad (2.28)$$

Curle showed that the dipole sources are most dominant for low Mach numbers.

#### 2.3.2.3 Quadrupole

This sources radiates sound less effectively than the dipole and is given by

$$\square^2 \rho = \frac{\partial^2}{\partial x_i \partial x_j} (\rho u_i u_j - \tau_{ij}) \quad (2.29)$$

where  $T_{ij} = \rho u_i u_j - \tau_{ij}$  is called Lighthill stress tensor. It can be noted that the viscos forces  $\tau_{ij}$  are mainly important for dampening sound waves and their importance for sound generation is negligible. The quadrupole source corresponds to to sound production due to the momentum transport  $\rho u_i u_j$  in the flow. The time average of this term is called Reynolds stress and is responsible for the added viscosity experienced in turbulent flow. The unsteady part of this term is the noise generating

term in the quadrupole source. This source term is caused by turbulence in the free shear layer. Hirschberg and Rienstra [12] describe this as two people fighting on a boat as these sources are more irregular. The dependence can be related to velocity and Mach number [13] as

$$p'_q \propto u^2 M^2 \quad (2.30)$$

The quadrupole will give less pressure fluctuations for  $M \ll 1$  but are significantly important for higher Mach numbers. This source term is the main source of noise from a high speed jet.

### 2.3.3 Computational Aeroacoustics (CAA)

This is the field of numerically computing the flow induced generation of sound. A direct simulation of this would involve solving the governing equations for flow and the propagation of sound. This would be more computationally demanding than DNS. Instead of using the direct simulations, acoustics analogies have been developed and widely used for the prediction of far field noise generated by aerodynamic noises [15]. This is a hybrid method which involves two steps. The first step is to calculate the flow field using computational fluid dynamics (CFD) methods. At high Reynolds number the cost of using DNS and LES are high. However, RANS provides only a mean flow information and not the instantaneous fluctuations that are required for the aeroacoustics analysis. In the next step, flow properties are measured and formulated as source terms for the acoustic analogies. The acoustics analogy in CAA is used to isolate the noise computation from the flow computation. An assumption made here is that the flow and acoustics are decoupled. More accurately this means that the propagation of sound doesn't affect the flow.

#### 2.3.3.1 Lighthill's acoustic analogy

The analogy method was first proposed by Lighthill [16, 17]. The Lighthill equation is obtained by first subtracting the divergence of the momentum equation (eq 2.4) from the time derivative of the continuity equation (eq 2.1) to obtain

$$\frac{\partial^2 \rho}{\partial t^2} = \frac{\partial^2}{\partial x_i \partial x_j} (\rho v_i v_j + p \delta_{ij} - \tau_{ij}) \quad (2.31)$$

Eq 2.22 can be expressed as

$$c_o^2 \frac{\partial^2}{\partial x_i^2} - \frac{\partial^2 p \delta_{ij}}{\partial x_i \partial x_j} = 0 \quad (2.32)$$

Subtracting eq 2.32 from eq 2.31 we get the Lighthill equation

$$\frac{\partial^2 \rho}{\partial t^2} - c_o^2 \frac{\partial^2 \rho}{\partial x_i^2} = \frac{\partial^2 T_{ij}}{\partial x_i \partial x_j} \quad (2.33)$$

where  $T_{ij}$  is the Lighthill stress tensor,

$$T_{ij} = \rho v_i v_j + (p - \rho c_o^2) \delta_{ij} - \tau_{ij} \quad (2.34)$$

This an inhomogeneous wave equation which describes the linear motion of sound waves generated by fluctuations in the flow. This is an exact equation and is valid as long as the flow is known at every point at every instant of time. Outside the turbulent region the acoustic wave propagation would be governed by the homogeneous wave equation. In this region the density and pressure act on a quiescent fluid with small perturbations and hence it can be expressed as

$$\begin{aligned}\rho &= \rho_\infty + \rho' \\ p &= p_\infty + p'\end{aligned}\tag{2.35}$$

The Lighthill equation can thus be expressed as

$$\frac{\partial^2 \rho'}{\partial t^2} - c_o^2 \frac{\partial^2 \rho'}{\partial x_i^2} = \frac{\partial^2 T_{ij}}{\partial x_i \partial x_j}\tag{2.36}$$

An analytical solution is obtained by applying Green's function which gives

$$\rho'(\mathbf{x}, t) = \frac{1}{4\pi c_o^2} \int_V \frac{1}{r} \frac{\partial^2 T_{ij}}{\partial x_i \partial x_j}(\mathbf{y}, \tau_r) dV(\mathbf{y})\tag{2.37}$$

where  $\mathbf{x}$  is the position of the observer in the far field and  $\mathbf{y}$  is the source location.  $\tau_r$  is the retarded time given as

$$\tau_r = t - \frac{r}{c_o}\tag{2.38}$$

where  $r = |\mathbf{x} - \mathbf{y}|$  is the distance between the source and observer. The left side of eq 2.37 corresponds to far field density fluctuations around a state of rest which is,

$$\rho'(\mathbf{x}, t) = \rho(\mathbf{x}, t) - \rho_\infty\tag{2.39}$$

Assuming an adiabatic process of sound propagation, the far field density fluctuations can be related to the far field pressure fluctuations by

$$p'(\mathbf{x}, t) = \rho'(\mathbf{x}, t) c_o^2\tag{2.40}$$

The sound pressure level can then be calculated for the observer using equations 2.37 and 2.40.

The assumption that the acoustic field doesn't affect the flow field is not always true. The acoustic field and flow field in reality are dependant on each other which can be seen by the Lighthill equation. The varies on the basis of when the two fields interact. For low Mach flows the interaction can be considered as one way coupled where the acoustics field depends on the flow field and not the other way round. In two way coupled the fields are dependant on each other.

This acoustic analogy was expended to include the effects of stationary wall within the flow by Curle and later for moving walls by Ffowcs Williams and Hawkings. These methods are explained later.

### 2.3.3.2 Curle Method- special case of FW-H

The Curle formulation generalizes the Lighthill equation to include rigid walls in the flow field [18]. The equation is given by [18, 19]

$$\square^2 p'(\mathbf{x}, t) = -\frac{\partial}{\partial x_i} (p' n_i \delta(f)) + \frac{\bar{\partial}^2}{\partial x_i \partial x_j} (T_{ij} H(f)) \equiv Q_{CUR} \quad (2.41)$$

The first term on the right corresponds to the noise induced by pressure perturbations in the boundary layer flow over the wall. The Lighthill stress tensor is neglected and the solution is given by

$$p'(\mathbf{x}, t) = -\frac{1}{4\pi} \int_{f=0} \left\{ \frac{\cos\theta}{r} \left[ \left( \frac{1}{c_o} \frac{\partial}{\partial \tau} + \frac{1}{r} \right) p' \right]_{ret} \right\} dS \quad (2.42)$$

The permeable surface in the FW-H method can be attached to the stationary wall. This will then give the above Curle equation. This makes this form of the Curle equation a special case of the FW-H method. For this thesis, this was the method that was adopted.



# 3

## Methods

This chapter will explain the methodology adopted in the thesis. With a brief introduction of the entire work flow, a description of each choice along with reason of each setting is given.

### 3.1 Workflow

The work flow starts with geometry creation followed by defining the flow domain. Based on the type of flow and the turbulence model used, the mesh requirements are obtained and a mesh is generated. Flow is simulated using Computational Fluid Dynamics (CFD), from which required properties are measured and exported for the acoustic solver. The method of solving the aeroacoustic problem is the hybrid method where flow and acoustic calculations are decoupled.

### 3.2 Geometry and Domain

The Ahmed body was defined by Ahmed et. al. in [20]. It is essentially a simplified representation of a car body. It neglects many of the details of a real car but gives a essential details of the flow features, typically the separation in the wake. This helps in studying important processes such as drag. Morel [21] and Hamed [20] were the first to show the significance of the slant in the rear of the car. This lead to the implementation of the three different types of rear geometries namely, the slant-back or the fast back, the bus or square back and the notch or sedan back. The only difference here is the rear which implies that the structures of the wake would be different. The difference in noise generated would hence be due to the differences in the wake.

#### 3.2.1 Geometry

Three geometries of the Ahmed body with different backs were chosen, namely the standard slant back, the notch back and the square back. The dimensions of each are the same with and are expressed in terms of height of the body. The height for the body was  $H = 0.297m$  Figures 3.1, 3.2 and 3.3 shows the side and rear view of the three different geometries. The slanted surface in the notch back is usually referred to as backlight. The horizontal surface is called the deck. The angle of the backlight used here is  $42^\circ$

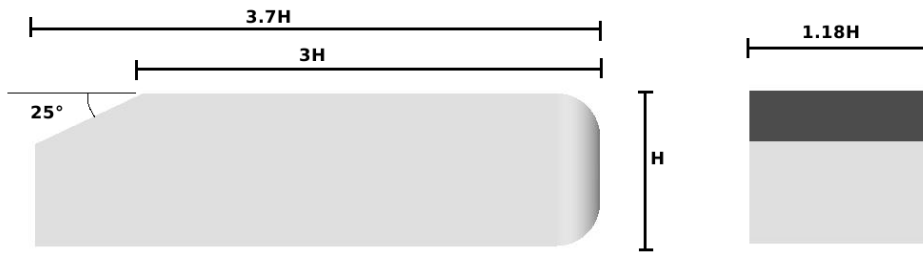


Figure 3.1: Slant-back



Figure 3.2: Notch-back



Figure 3.3: Square-back

### 3.2.2 Computational Domain

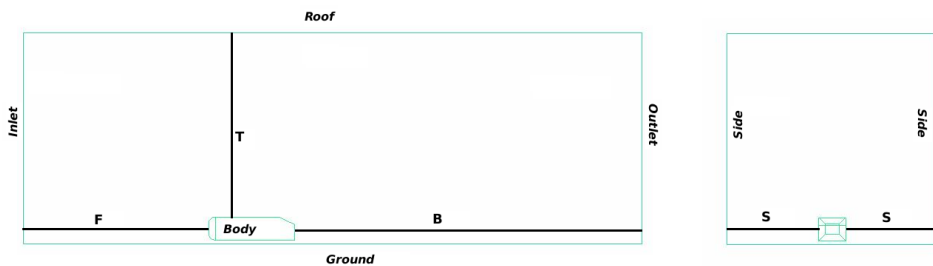


Figure 3.4: Domain

The dimensions of the wind tunnel domain is also expressed in terms of the height  $H$  of the Ahmed body. The distance of the inlet to the front of the body is  $F = 8H$ . The distance of the rear of the body to the outlet is  $B = 15H$ . The height from the top of the car to the roof is  $T = 5H$  to  $T = 8H$ . On either side of the car the distance is  $S = 3H$  to  $S = 4H$ . The distance from the bottom of the car to the ground is  $h = 0.17H$ .

### 3.3 Mesh

The mesh was made using ANSYS ICEMCFD. Hexahedral cells are used to make a structured mesh in this software. Here the criteria for making a mesh for LES and aeroacoustics are discussed.

#### 3.3.1 Mesh requirements

##### 3.3.1.1 For LES

The cell sizing near the wall of the body is determined by boundary layer region to be resolved. These quantities are specified in terms of dimensionless namely, the wall normal resolution  $n^+$ , streamwise resolution  $s^+$  and the spanwise resolution  $l^+$ . These values are calculated by

$$\begin{aligned} n^+ &= \frac{u_* n}{\nu} \\ u_* &= \sqrt{\tau_w / \rho} \approx 0.05 V_\infty \end{aligned} \quad (3.1)$$

where  $n$  is the distance from the wall,  $\tau_w$  is wall shear stress,  $\nu$  is kinematic viscosity. The requirements for LES are  $n^+ < 1$ ,  $l^+ < 30$  and  $s^+ < 100$ . Based on these the cell size are calculated and specified for the near wall.

##### 3.3.1.2 For aeroacoustics

The mesh size are based on the recommended at least 10 cells per acoustical wavelength [22]. That can be represented as as

$$\Delta = \frac{\lambda}{10} \quad (3.2)$$

where  $\lambda = a/f$ ,  $a$  is speed of sound and  $f$  is frequency. So a frequency of 1000Hz requires a  $\Delta \leq 0.034m$ . However the LES mesh is used for the aeroacoustic calculation. The contribution of pressure fluctuations of small eddies are to be included for far field noise calculation which can be only resolved by the LES mesh.

#### 3.3.2 Mesh details for geometries

The meshes were made for a Reynolds number 10000. The free stream velocity was calculated to  $V_\infty = 0.508m/s$  based on the height of the geometry. The above requirements for LES were kept and the first cell height was specified within the  $n^+$

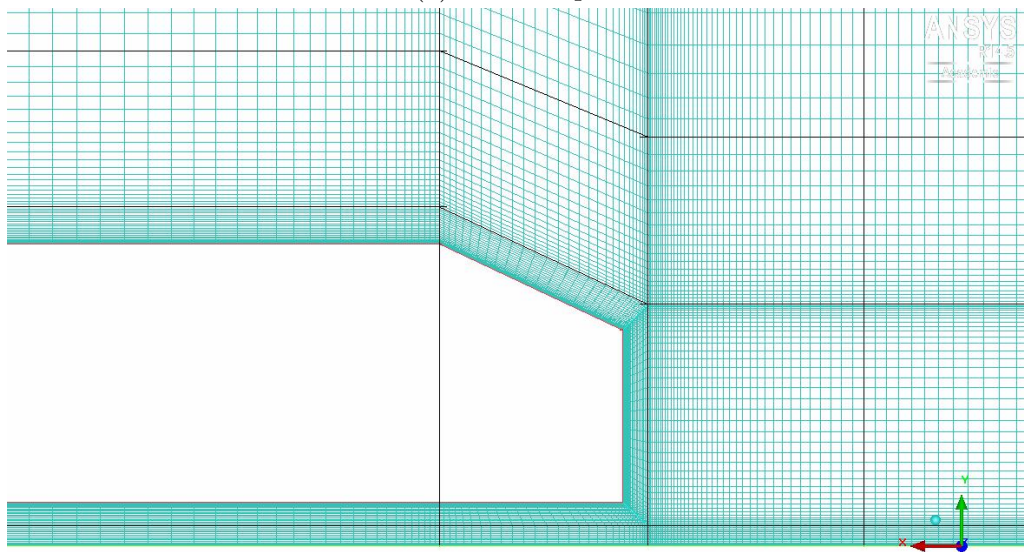
### 3. Methods

---

of 1. The aspect ratios of the cells at sharp corners are important and a ratio of no more than 3:1 were used. No cell in the domain of the computational grid was larger than  $0.5H$ . As the Ahmed body is a symmetric geometry, the mesh made was also symmetric. The blocking transition and cell growth were kept smooth from the surface of the body to the walls of the wind tunnel.



(a) Contour plot



(b) Surface plot

Figure 3.5: Temperature plots, Gauss Seidel

The table 3.1 gives some of the details of the mesh that were made for each body.

<i>Body</i>	<i>Slant</i>	<i>Notch</i>	<i>Square</i>
<i>No of cells</i>	3376539	3132744	3634537
<i>Cells on Body</i>	22654	28278	24590
<i>Surface area (m<sup>2</sup>)</i>	1.537	1.540	1.585
<i>Determinant 3x3x3</i>	0.887	0.675	0.853

Table 3.1: Mesh details

## 3.4 Numerical setup for CFD

The Large Eddy Simulations were done using AVL FIRE. This section will describe the setting used for the CFD simulations.

### 3.4.1 Transient

The data required for the aeroacoustic calculation are the unsteady pressure fluctuations on the surface of the body of the generic car. Therefore transient simulations were required. The time step size  $\Delta t = 0.001$  was used based on the CFL number. The criteria for this was

$$CFL = \frac{V_{\infty} \Delta t}{\Delta x} < 1 \quad (3.3)$$

where  $V_{\infty}$  is the free stream velocity,  $\Delta x$  is the smallest cell size.

### 3.4.2 Incompressibility

For low Mach numbers, typically  $M < 0.3$  air can be assumed to be incompressible. This is a good approximation for flow problems, however sound propagation is caused by compressibility of air. In a compressible flow the sources of sound at a given instant will contain both the effects of turbulence and acoustic waves. This is expressed in the right hand side of the Lighthill and Curle equation in the Lighthill tensor. Since we are neglecting the Lighthill stress tensor and using the Curle equation which depends only on pressure fluctuation on the surface of the body the incompressibility criteria holds.

### 3.4.3 Boundary conditions

The boundary conditions used are shown in the table

<i>Inlet</i>	inlet/outlet at velocity at $V_\infty$
<i>Outlet</i>	inlet/outlet with gradient = 0
<i>Body</i>	Wall with velocity 0
<i>Ground</i>	wall with velocity $V_\infty$
<i>Roof</i>	symmetry
<i>Sides</i>	symmetry

Table 3.2: Boundary conditions

### 3.4.4 Data for Aeroacoustics

The data required for the aeroacoustics calculations are the pressure fluctuations for each time step for each cell on the surface on the car, the coordinate of each cell, each component of the normal and the area of the cell. The cell data is obtained from the 2D output from AVL Fire. The pressure is extracted using the `usetim.f` user defined code for monitoring points. The total time for which the pressure data is obtained is minimum six flow passages over the length of the car body. The total time chosen was 15s which corresponds to roughly seven flow passages.

## 3.5 Acoustics solver

The solver is an in house code [23] in FORTRAN that gives the analytical solution of the Curle equation and calculates pressure at a specified positions. The coordinates of these are selected as shown in the figure 3.6. Here only one of the geometries are shown. The same was done with the other two geometries. These pictures are an exaggeration just to visibly present the orientation of the points with respect to the body. In reality the points are much further away from the body.

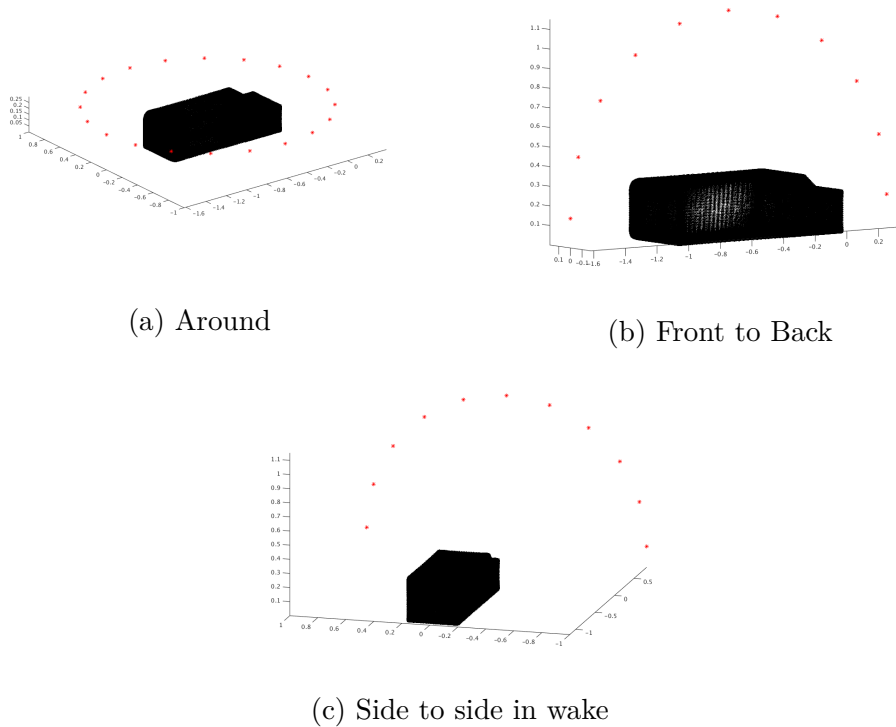


Figure 3.6: Mic Positions

Figure 3.6a show the points around the body at same height of the body,  $10m$  away. Figure 3.6b show points from front to back and over the body at a distance of  $10m$ . Finally figure 3.6c show points from side to side and over the wake of the car at distance  $1m$  from the rear of the body with a radius of  $10m$ . Matlab was used to make these coordinate points.

### 3.6 Postprocessing

The CFD simulations analysed using Enight and the aeroacoustics data is analysed using Matlab. The sources of sound is analysed by comparing near field pressure fluctuations from the CFD simulation data to the far field propagation of sound. The near field pressure is plotted from the CFD simulation at certain monitoring points. Figure 3.7 shows an example of the way the monitor points were located for the notch back. Similar to this the monitor point were placed in the other two geometries.

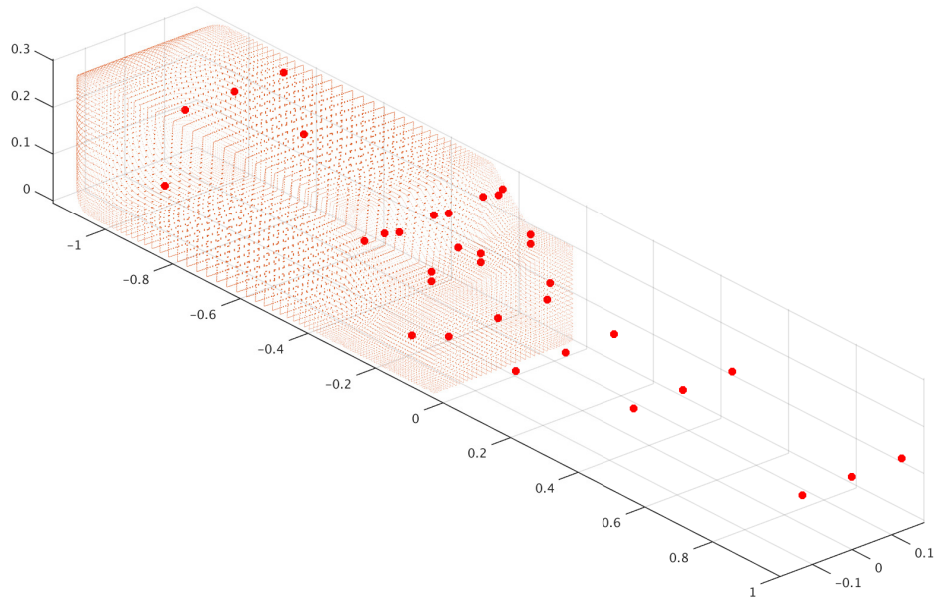


Figure 3.7: Monitor points for notch back

The pressure is plotted in the frequency domain for both near field and far field. The dominating frequencies, i.e frequencies with the highest peak are then checked. This helps identify the location of the sources for the sound. Codes for calculating Sound Pressure Level(SPL) and Overall Sound Pressure Level (OASPL) are given in the appendix.

# 4

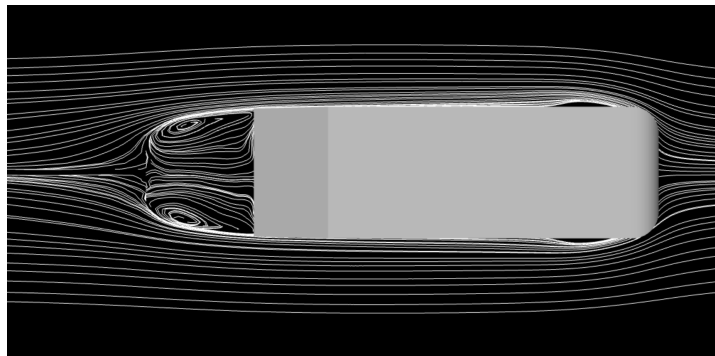
## Results

Here the results obtained from the CFD simulation and aeroacoustic calculations are presented.

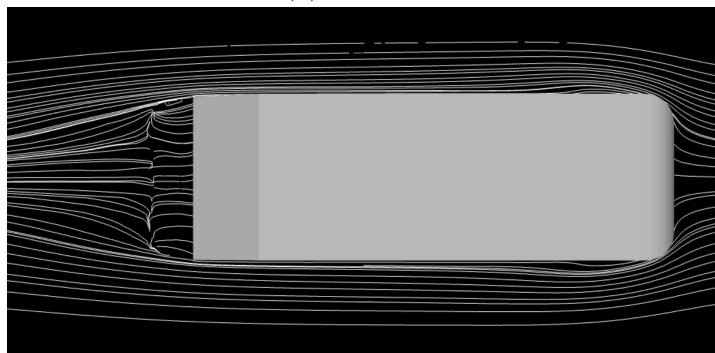
### 4.1 Computational Fluid Dynamics

For each case the a Reynolds number of 10000 was chosen. Each body being of the same height had the same inlet velocity of  $0.508m/s$ . The simulation was carried out for roughly 4 wind-tunnel flow passages to ensured the flow was averaged correctly. The aver ageing was done for the last 2.5 flow passages. Each flow passage was about 15.5 seconds.

#### 4.1.1 Slant-back



(a)  $Y = 0.1m$



(b)  $Y = 0.2m$

Figure 4.1: View from top

Figure 4.1 show flow average velocity streamlines for planes specified at different heights. Figure 4.1a is roughly at the middle of the height of the back portion of the car. Symmetric circulations of the flow can be seen here. This is an indication that the simulation has been averaged for sufficient time.

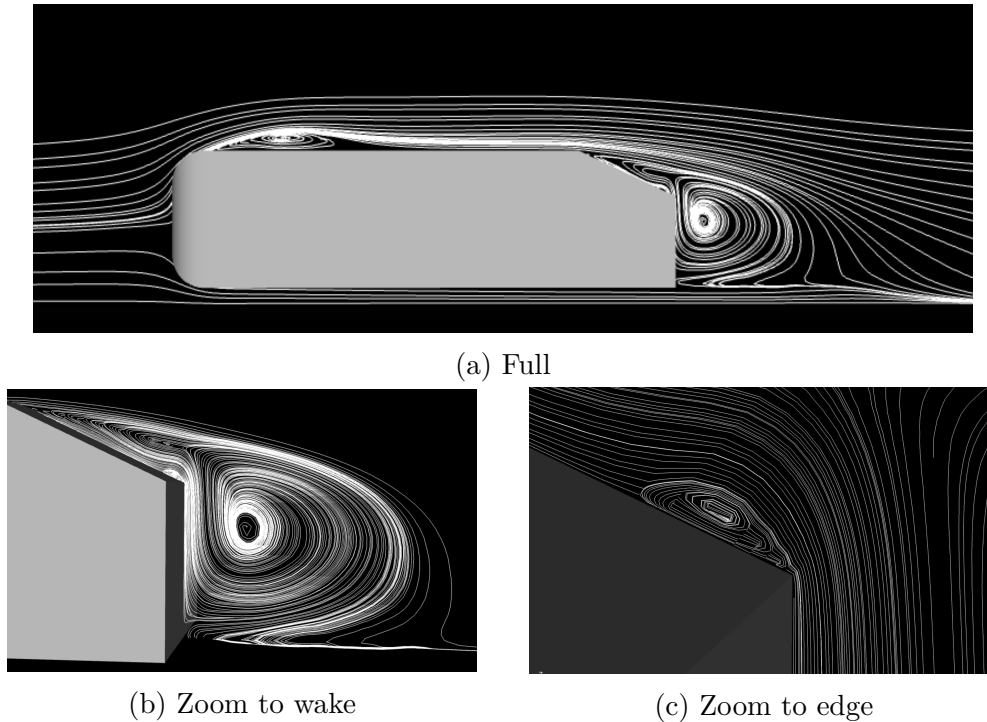


Figure 4.2: Side view

Figure 4.2 show the average velocity stream line for a plane at the middle of the car. On the top of car in figure 4.2a a recirculating bubble can be seen. This represent flow that is separated and reattached. The wake is shown in figure 4.2b where the flow recirculates along the back and the slant surfaces of the car. Zooming into the edge between the back and the slant surface a counter rotating bubble can be seen in figure 4.2c.

Figure 4.3 show flow average velocity for planes specified at different distance along the length of the car. It can be seen how the flow moves along the length and down the slope of the slant. The vortices on each side of the car become smaller as it moves towards the end of the car. No prominent vortices can be seen on the slant region. Figure 4.3a is closer to the front of the geometry while the rest are on the slant.

Figure 4.4 shows the relative pressure at an instant for each view. Regions where the flow reattaches is visible on the top and sides, closed to the front of the body.

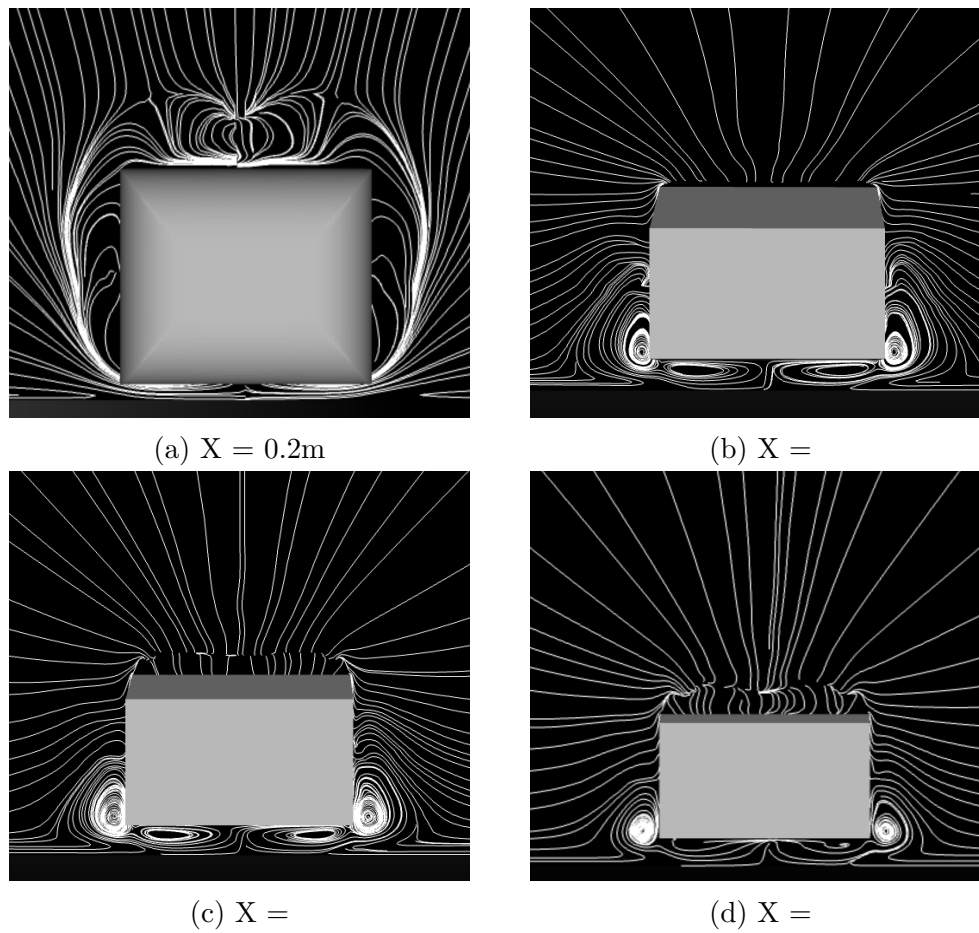


Figure 4.3: View from front/back

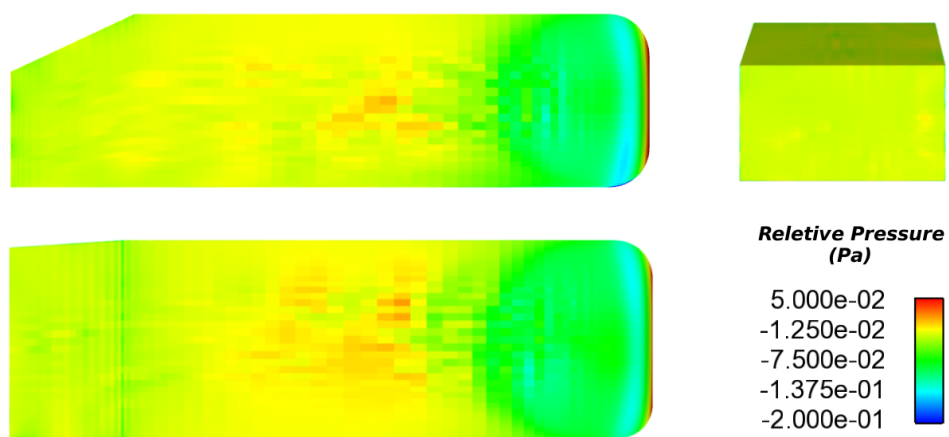
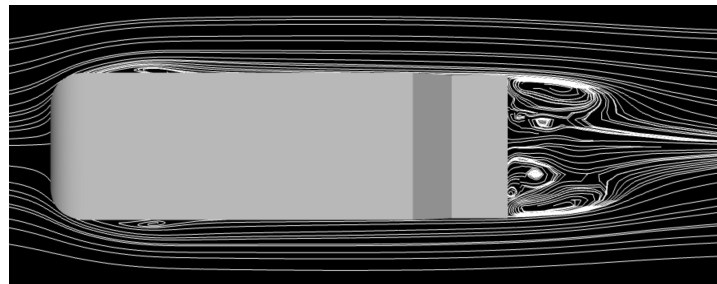
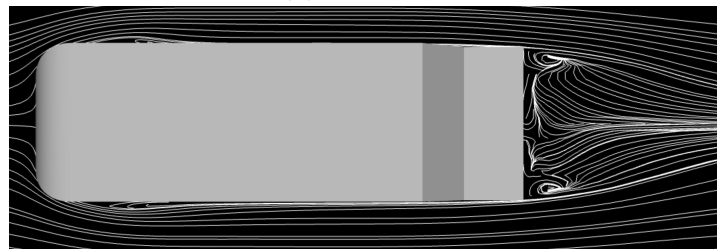


Figure 4.4: Instantaneous pressure

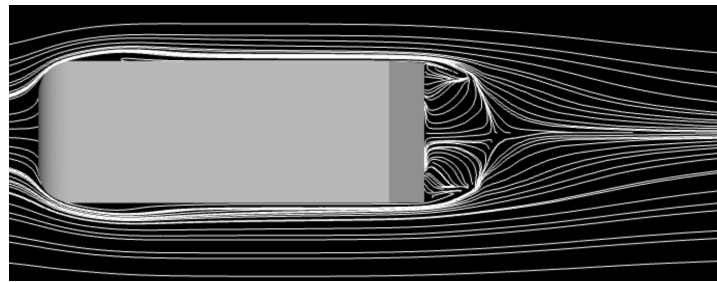
### 4.1.2 Notch-back



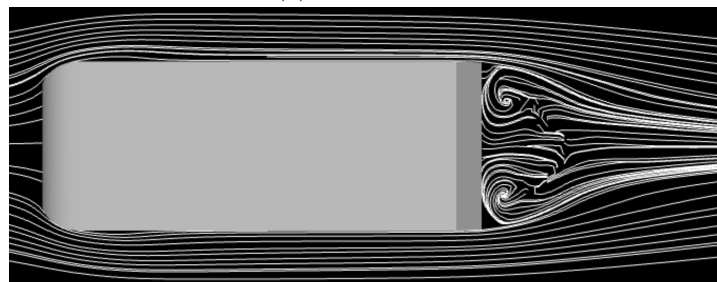
(a)  $Y = 0.1\text{m}$



(b)  $Y = 0.2\text{m}$



(c)  $Y = 0.21\text{m}$



(d)  $Y = 0.25\text{m}$

Figure 4.5: Top view

Figure 4.5 show the flow averaged streamlines of velocity for planes specified at different heights of the geometry. These are located at the middle of the back, just below the deck, just above the deck and midway to the backlight respectively.

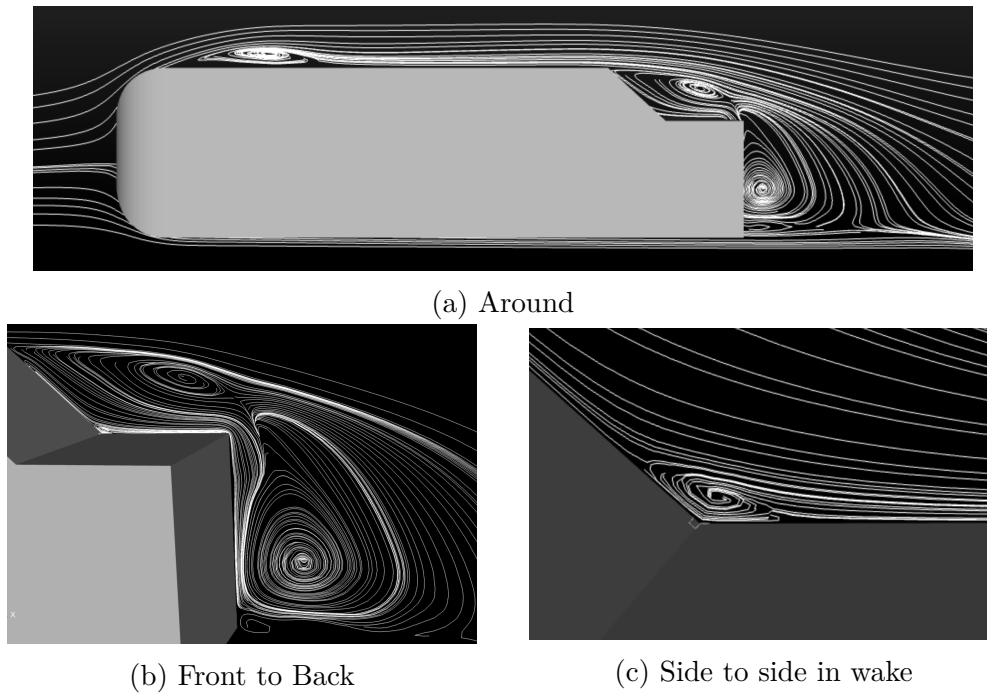


Figure 4.6: Side view

Figure 4.6 show the average velocity stream line for a plane at the middle of the car. It can be seen than part of the flow recirculates along the back, the deck and the backlight of the car. There is also two separate circulation of flow just behind the back and above the deck which can be seen in figure 4.6b. Also a small counter rotating vortex can be seen between the backlight and deck which is shown in figure 4.6c.

Figure 4.7 show average velocity streamlines for different planes along different positions along the length of the car. The vortices along the the bas of the car seem to be of the same size as they move along the length of the car. There is vortex formed at the end of the backlight which is shown in figure 4.7c. Figure 4.7a is in close to the front of the car, while figures 4.7b, 4.7c and 4.7d are on the backlight, between the backlight and deck, and on the deck of the car respectively.

Figure 4.8 shows the relative pressure at an instant for each view. As in the previous before, regions where the flow reattaches is visible on the top and sides, closed to the front of the body.

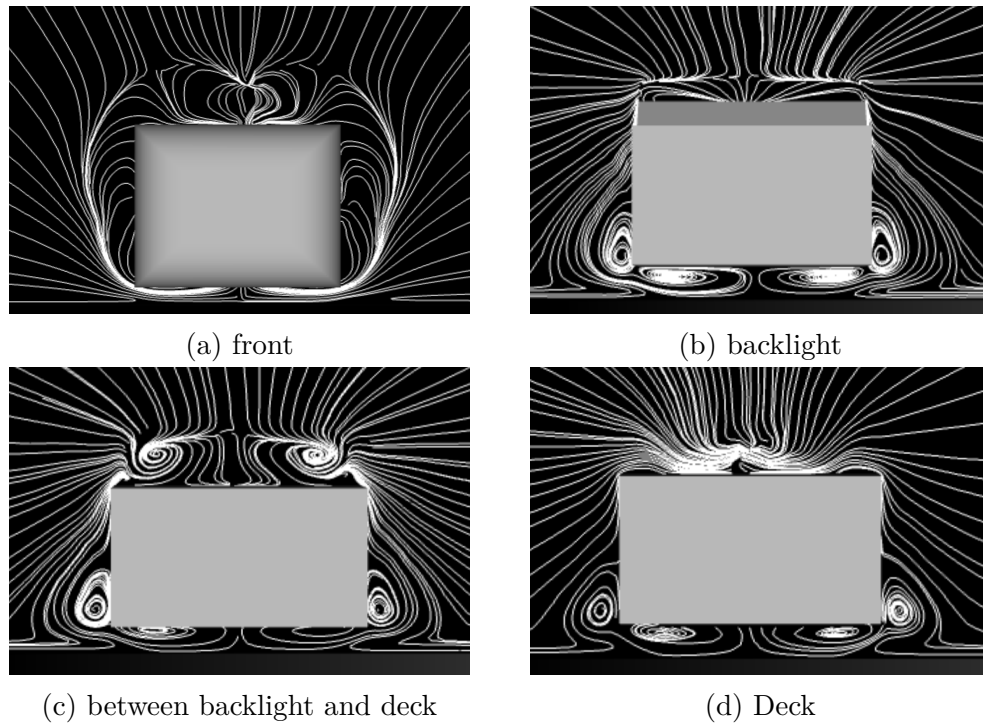


Figure 4.7: Front/back view

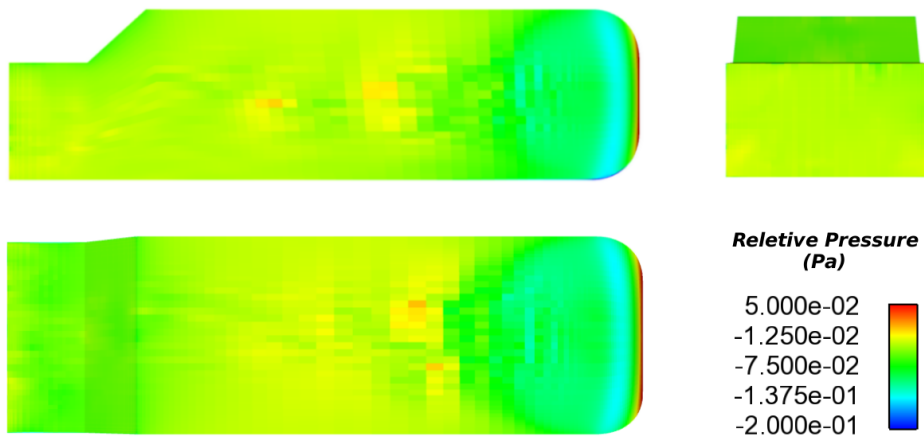


Figure 4.8: Instantaneous pressure

### 4.1.3 Square-back

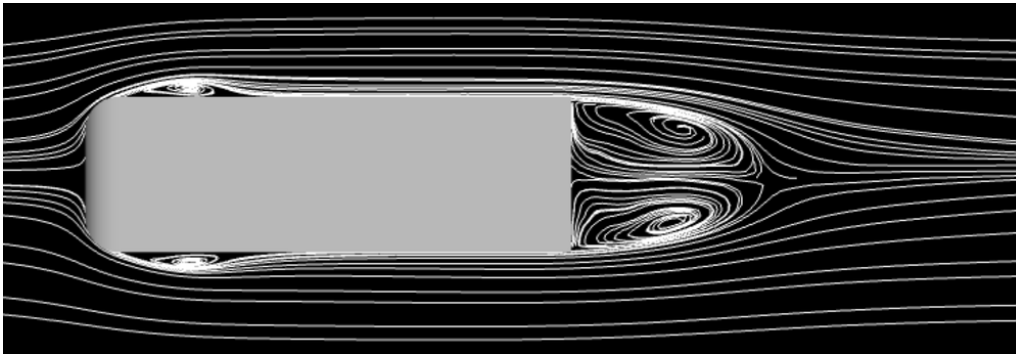


Figure 4.9: Top view

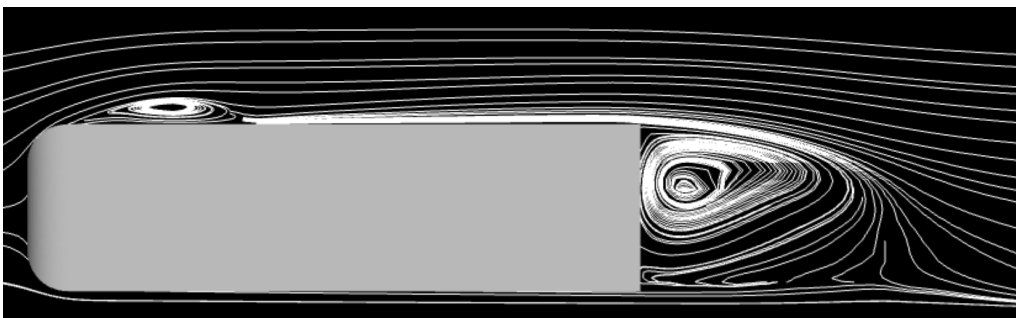


Figure 4.10: Side view

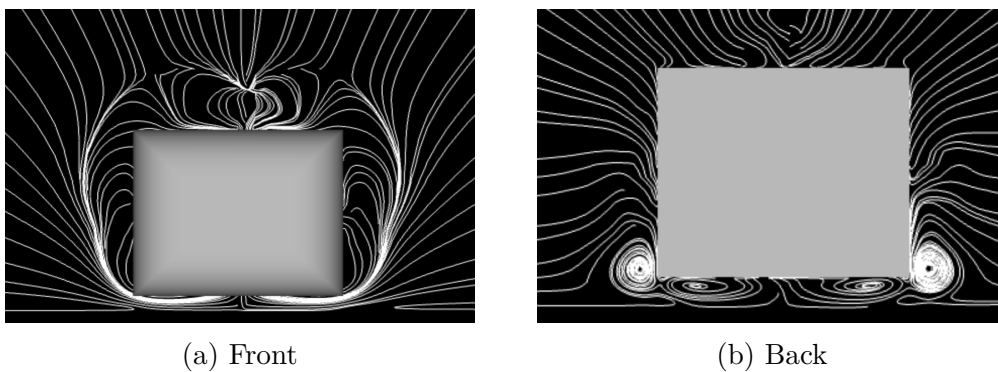


Figure 4.11: Front/back view

Figure 4.11a show the flow averaged velocity streamlines for a plane at a height of  $0.15m$ . Symmetry in the flow is again visible here along with two separation bubbles on either side of the body close to the front of the car. Figure 4.10 shows the same for a plane at the middle of the body and figure 4.11 show the same for a plane in the front and at the back of the car body.

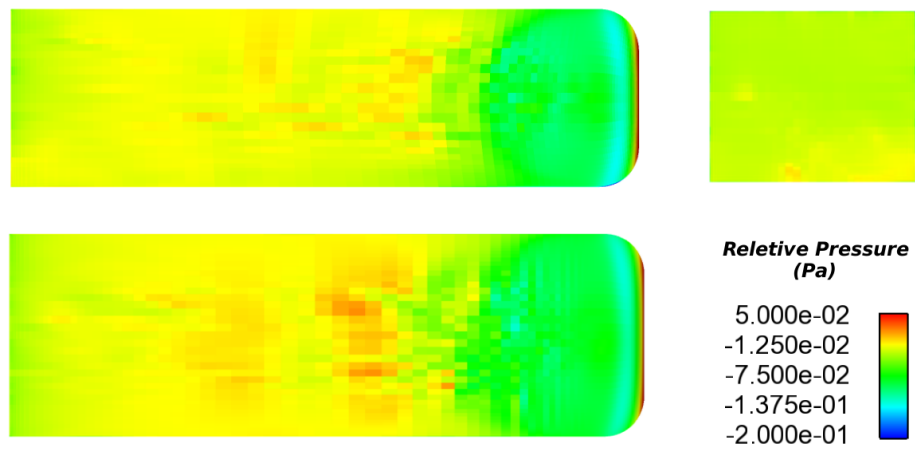


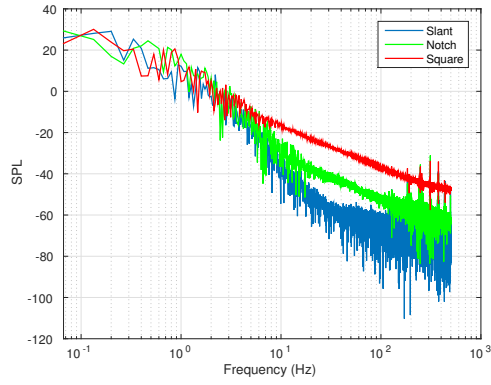
Figure 4.12: Instantaneous pressure

Figure 4.12 shows the relative pressure at an instant for each view as for the previous two cases. Regions where the flow reattaches is visible on the top and sides, closed to the front of the body which are similar to the other two bodies in figures 4.4 and 4.8.

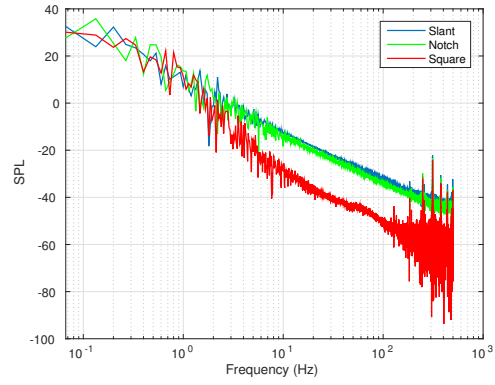
## 4.2 Aeroacoustics

### 4.2.1 Sound Pressure Level (SPL)

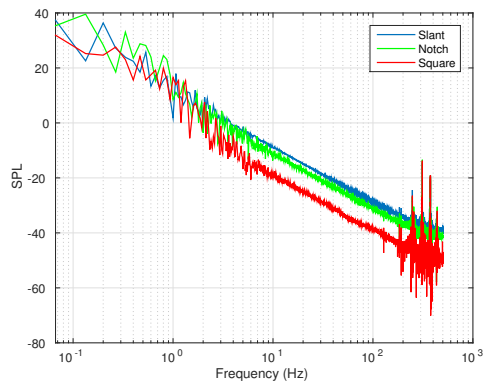
The SPL was calculated for all the points shown in Fig. 3.6.



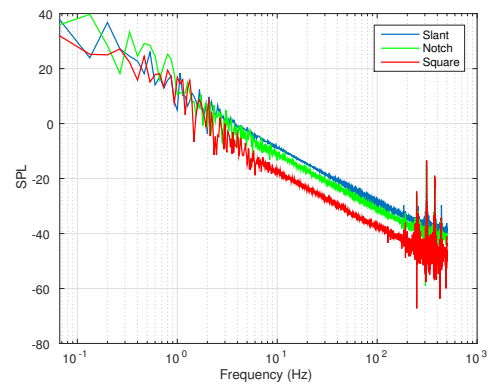
(a) Wake, 10m



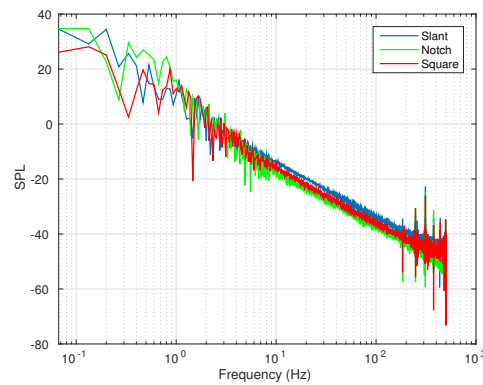
(b) Wake, 10m at angle with the ground



(c) Wake, 10m above the ground



(d) 10m directly above geometry



(e) Front, 10m with angle with ground

Figure 4.13: SPL for selected mic positions

In Fig. 4.13 the slant, notch and square back geometries are represented by blue, green and red lines respectively. Figure 4.13a is the SPL for a point located 10m directly behind the the body at the same height of the body. Figure 4.13b is behind the body 10m away but an angle of  $36^\circ$  with respect to the ground. Figure 4.13c represents another point behind the body 1m away at a height of 10m. Figure 4.13d is a point 10m directly above the body and finally figure 4.13e is 10m away at angle of  $36^\circ$  in front of the body.

## 4.2.2 Overall Sound Pressure Level (OASPL)

Instead of plotting and analysing the SPL for each point in Fig. 3.6, the overall sound pressure level can be calculated. This is the summation of the sound levels and shows the directivity of sound. Directivity is the measure of the directional characteristic of a sound source. These are calculated for each position in the far-field and plotted in a polar format.

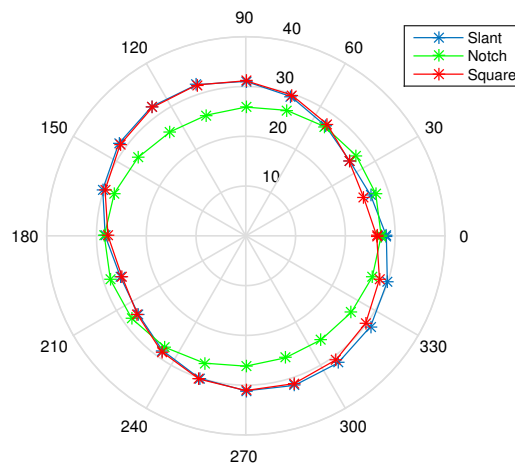


Figure 4.14: OASPL around the car

Figure 4.14 shows the OASPL for the points placed around the car as shown in figure 3.6a with a radius of 10m. The slant, notch and square geometries are represented with blue, green and red lines respectively. Here  $0^\circ$  is at the front of the car and the view is as seen from top. Similarly figure 4.15 correspond to the OSAPL measured from front to back as in figure 3.6b at a distance of 10m from the body.  $0^\circ$  here is at the front of the body. Finally figure 4.16 corresponds to points as shown in figure 3.6c with a radius of 10m. Here  $0^\circ$  is to the right, when facing the front of the body.

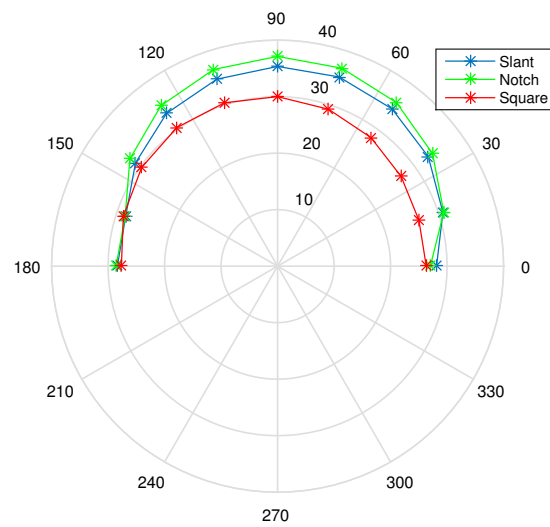


Figure 4.15: OASPL front to back

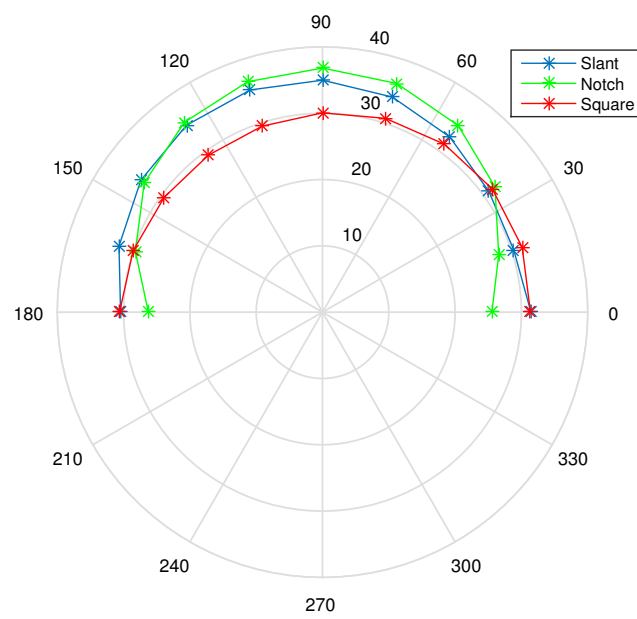


Figure 4.16: OASPL side to side in wake



# 5

## Discussion

Here the results will be analysed and the differences will be discussed in flow and noise calculations. Finally the near field flow data will be correlated to the far field noise calculation.

### 5.1 Comparison of flow

The only difference in the shape of Ahmed bodies are the backs. This means that the difference in the flow structures are purely to do with the difference in the geometry. The flow is therefore the same in the front of the car and this is confirmed by figures 4.3a, 4.7a and 4.11a which of course is expected. This can also be observed from the instantaneous pressure contours shown in figures 4.4, 4.8 and 4.12. Another similarity in the flow can be seen at the back, which are the presence of vortices close to the base, on either side of the body which are seen in figures 4.3 (b),(c),(d), 4.7(b),(c),(d) and 4.11 (b).

Figures 4.2, 4.6 and 4.10 show the flow recirculation in the wake of the car body as seen from the side. The square back has a single large rotation pattern in the wake which moves up the entire length of the back. The slant back has two flow circulations. One large one where the flow move up the vertical back and slant surface of the car. The second is the small counter rotating flow on the edge between the vertical back and slant surface. The large recirculation pattern separates when it moves up the back to the slant creating this second counter recirculating. The notch back has four recirculation patterns. The first being the largest and similar two the previous two case where the flow travels along the vertical back, deck and backlight surface of the body. Two recirculation are resent inside this structure. One which is behind the vertical back and the other above the deck. A small counter recirculation is seen at the edge between the deck and the backlight surfaces.

Figures 4.1, 4.5 and 4.9 show the flow pattern from the top view. It can be seen in the figures 4.1a and 4.9 for the slant and square back bodies respectively that the flow is similar behind the vertical back surface. However for the notch back in figure 4.5a the flow behind the vertical surface is quite different. There is a presence of more than one vortex on either side of the body. Comparing the flow for the slant and notch back over the slant surfaces in figures 4.1b and 4.5(c), (d) there are prominent recirculation patterns in the notch back while there are none in the slant back. The same can be seen from the rear views from figures 4.3c and 4.7c

This implied that the the flow in the notch back is more complicated than the other two cases. The presence of these vortices shown in the wake of the notch

back would contribute to more pressure fluctuations on the surface of the deck and backlight of the notch-back.

## 5.2 Comparison of Noise

From figure 4.13 for each point the low frequencies are similar for each geometry, but based on the location of the point the higher frequencies vary. For a point in directly behind the car as in figure 4.13a the sound level for the square back is higher than that for the notch and slant back. This is because the vertical back surface of the square back is larger and hence contributes to a higher sound level. Similarly if we look at a point at behind the car at an angle of  $36^\circ$  with respect to the ground (along the length of the car) as in figure 4.13b, the sound levels are higher for the notch and slant back compared to the square back. Following the same reasoning the for a point in front of the car at an angle of  $36^\circ$  should in principle have similar sound levels. This is seen in figure 4.13e.

It is clear that the sound levels measured depend highly where the points are placed with respect to the car. This can also be seen from the overall sound pressure level plots. Figure 4.14 shows higher sound levels for the slant and square back on either side of the body than the notch back. That is because there is more surface area for slant and square back that contributes to sound level. There is an asymmetry in this figure. The reason for this is that the time for which the pressure were measured was not long enough. So the contribution for large scale eddies is missing. It can be seen that the overall noise levels for notch and slant back are higher in figures 4.15 and 4.16 compared to the the square back.

## 5.3 Identifying sources

The sources for the sounds can be identified by plotting the pressure fluctuations in the near field from the CFD simulation and comparing those to the pressure fluctuations in the far field calculated from the aeroacoustic solver.

### 5.3.1 Slant-back

For points in the far field above the car, the largest peak frequency observed is 0.2001 Hz. A monitoring point specified on top of the car also shows a peak at 0.2 Hz. This is shown in figure 5.1.

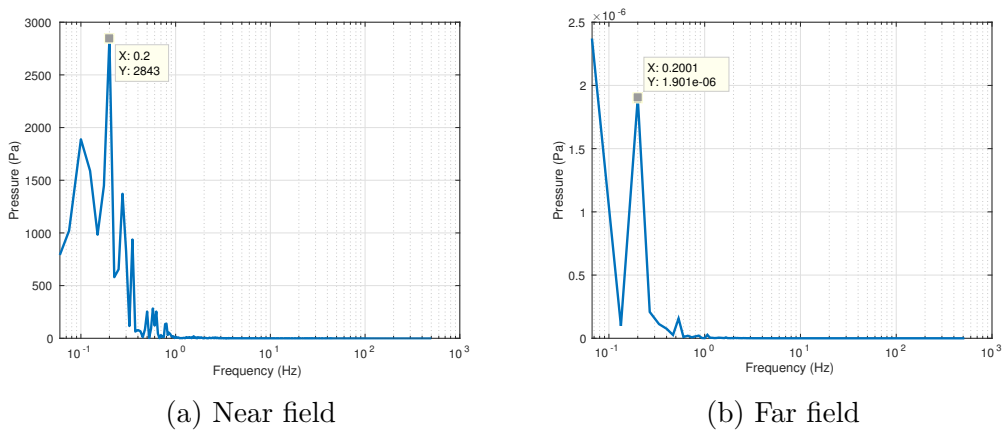


Figure 5.1: Pressure in spectra on top of body

The reason for this strong peak is the separation bubble on top of the car. The flow separated from the front and reattaches on the top interacting with the surface of the car.

In the far field, for a microphone located behind the car, a secondary peak frequency is found with 0.3335 Hz. This can be seen in figure 5.2.

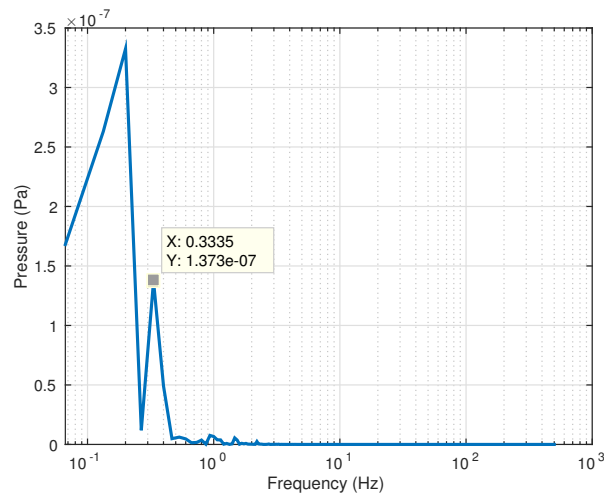


Figure 5.2: Far field noise, wake

A frequency of 0.3655 Hz and 0.3845 Hz were found for monitoring points located slightly above the surface in the slant region but on either side of the body, close to the edge. These two are shown in figure 5.3

## 5. Discussion

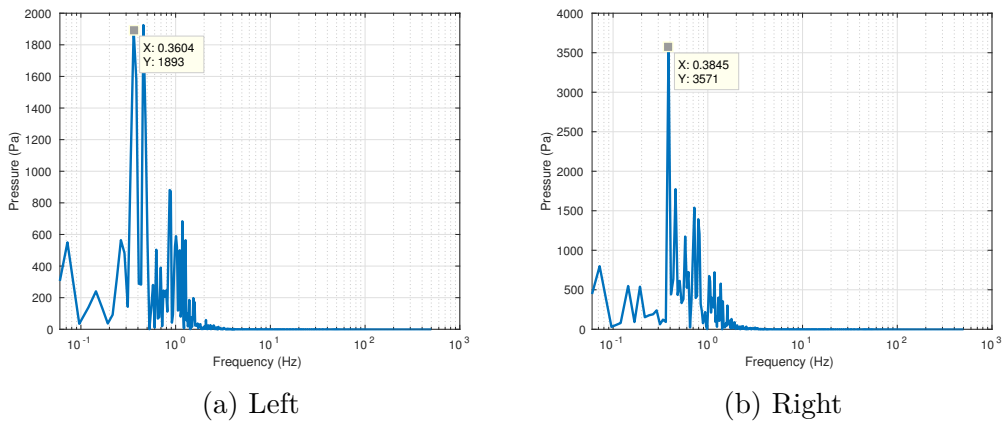


Figure 5.3: Near field on top of slant region

Also a frequency of 0.3364 Hz were found for points located in the wake. Figure 5.4 shows the near field pressure from CFD for three points located in the wake. This is the vortex shedding frequency. This suggests that the vortex shedding is a source for sound.

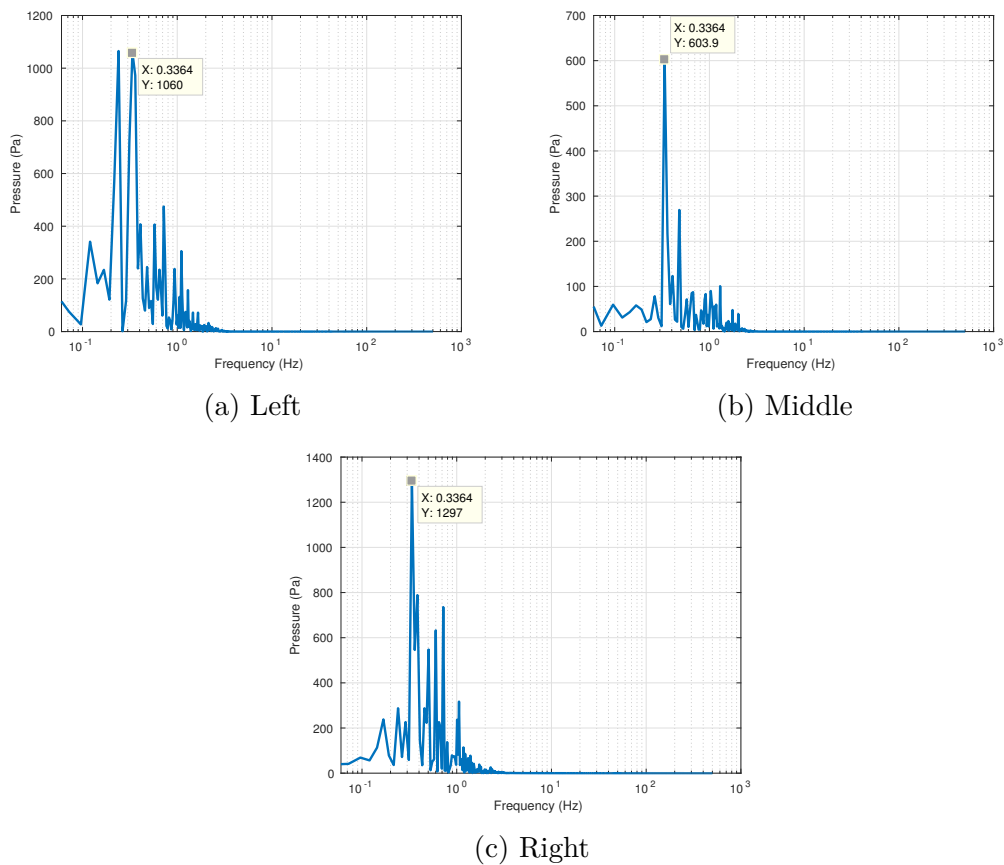


Figure 5.4: Near field in wake

Finally a small notable peak of 0.5336 Hz was found for a microphone located in the wake but 10m above the ground in the far field. A frequency of 0.5527 Hz was found from the near field data for a point on the slant of the car. These are shown in figure 5.5.

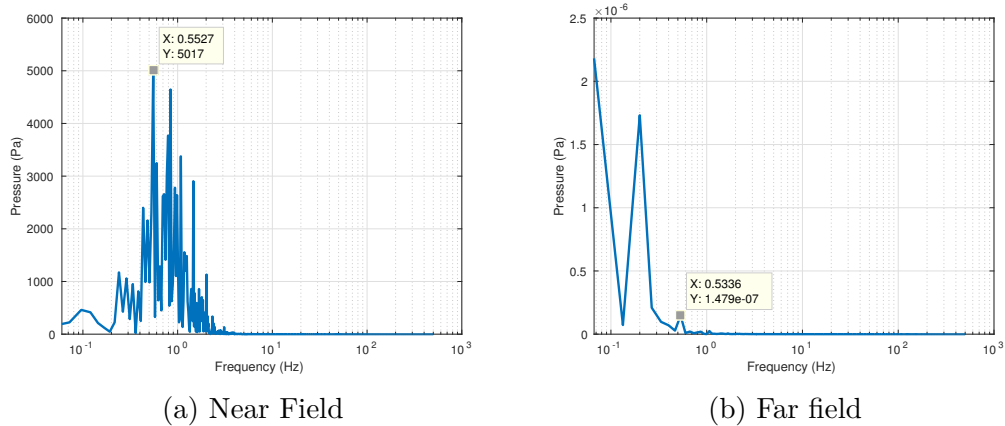


Figure 5.5: Pressure in spectra

### 5.3.2 Notch-back

For microphone points above the car a frequency of 0.1334 Hz is observed. Monitoring points on the top of the car show a frequency of 0.1194 Hz.

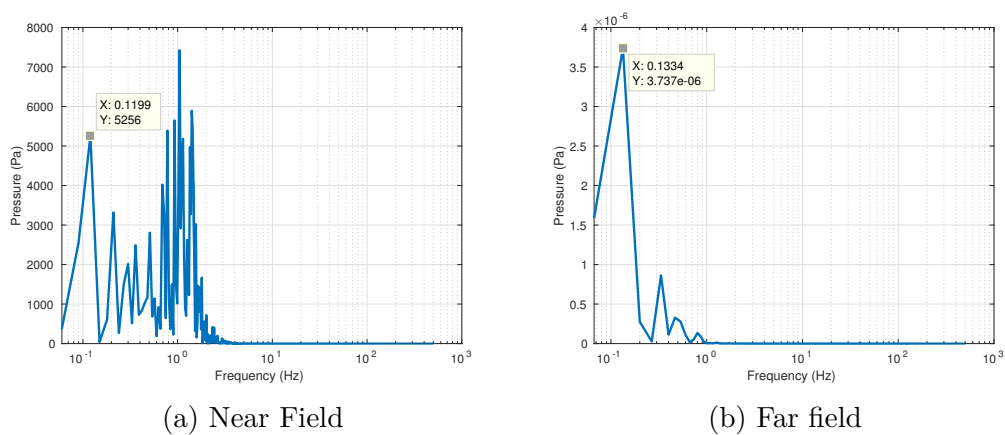


Figure 5.6: Pressure in spectra

In the far field above the car body a second peak is observed with a frequency of 0.333 Hz. Figure 5.7 shows this peak.

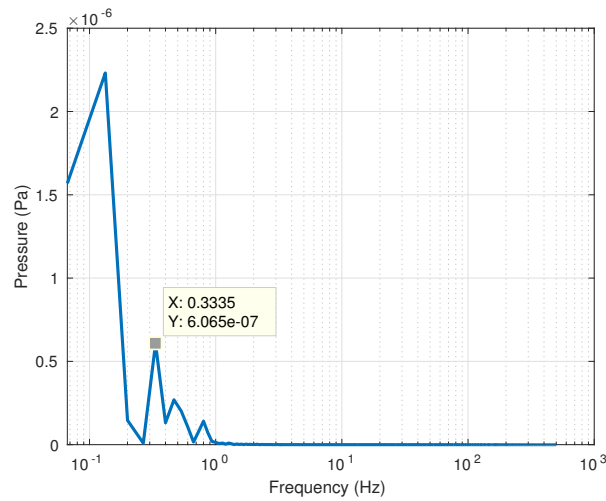


Figure 5.7: Far field noise, top

Also a secondary frequency of 0.466 Hz is observed in the far field noise for microphones located above the rear end of the car which is not present in the front. This can be seen in figure 5.8

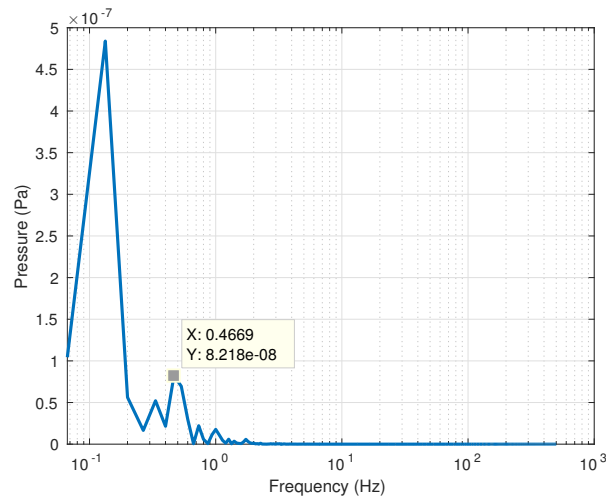


Figure 5.8: Far field noise, wake

A frequency of 0.3598 Hz and 0.4797 Hz is observed at the deck which can be seen in figure 5.9

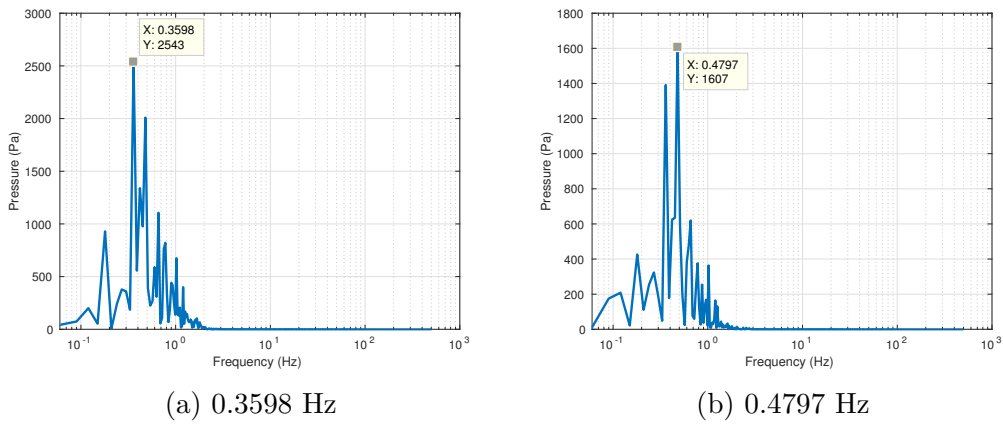


Figure 5.9: Pressure in spectra on deck

A frequency of 0.4497 Hz in the wake from the near field data.

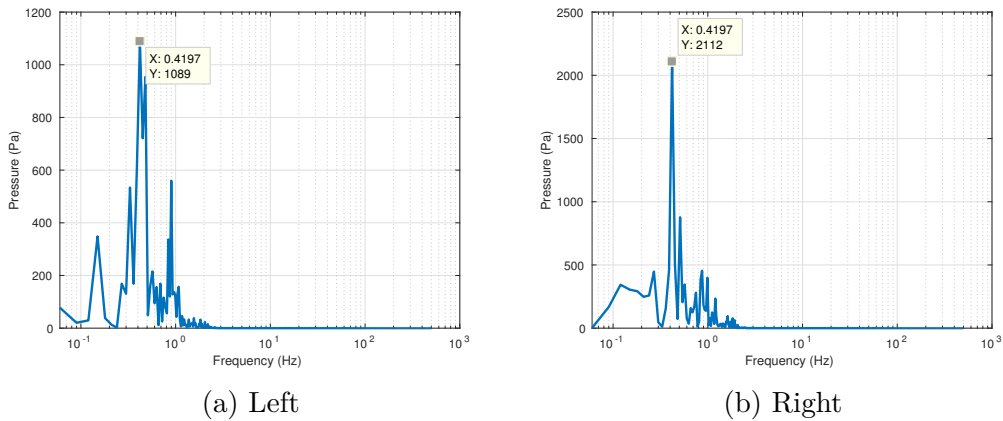


Figure 5.10: Pressure in spectra

It is important to note that the near field measurements are single points in the flow field but the far field noise data are measured from the overall contribution of pressure fluctuations from the surface of the body. Therefore the peak frequencies that correlate do not imply that the near field measurement are the point sources for the sound. They identify the region of the sources of sound. This explains why there is a slight difference in the numeric value of the peak frequencies from near field and far field data.



# 6

## Conclusion

To summarise the work, a hybrid computational aeroacoustic approach was used to analyse sound generated from the wake of the car using three different Ahmed bodies. The method involved using AVL Fire for the Large Eddy Simulations, which was the first step. The aeroacoustics problem was solved using the Curle method implemented in the in-house code [23]. The Curle equation was solved analytically using the pressure measured at the surface of the car body. This along with the surface normal and coordinates of the cell were imported from the CFD simulation.

Few assumptions were made and these were

- Ignoring the Lighthill Tensor: this term in the acoustic analogy equation accounts for the sound sources found in the volume of the turbulence. The Curle equation involves these sources and the the sources due to the interaction of the fluid with a solid surface. Since the volume source terms are scaled with  $u^2M^2$ , their effects are neglected in the present study, in which M is the Mach number. The velocity is extremely low the Lighthill tensor can be ignored;  $u^2M^2$  is of the order  $10^{-7}$ .
- Incompressibility: For low Mach number flows the flow can be considered as incompressible. However for sound propagation, the air must be compressible. However since we use the Curle acoustic analogy and only require pressure fluctuations the flow can be considered incompressible.

Some conclusions can be drawn from the results.

- From the CFD simulation the difference can be clearly seen in the wake region. Since the Curle method uses only pressure fluctuations on the surface of the geometry it would be expected that than the Notch back would generate more sound from the separation.
- Although the velocity is low there are clear differences observed in the noise generated. These are observed in the OASPL plots. The differences in the noise levels depend on where they are measure with respect to the car. Perpendicular distance to the surface of measurement show theses differences.
- Depending on the location of the observer, the noise levels would vary. Therefore it is can be said which geometry produces the most noise.
- There is more noise generated from the front of the car than the wake.

- The OASPL of the square back is asymmetric. This is due to the length of the data used for the calculation. The contribution of the low frequency need to be accounted. Using the data measured for a longer time shows a more symmetric OASPL.
- The sources of sound can be identified by comparing the spectra of pressure in the near field from the CFD simulations to the far field from the aeroacoustic solution. This gives an idea as to the general region where the source of sound exists.
- As expected the noise generated is not audible to the human ear. But this study is for developing a method for solving the problem and is a basis for future studies.

## Future work

- Validating the CFD simulation to experimental data. If the CFD simulations can be validated the aeroacoustic data is also accurate. The aeroacoustic analogy is solved analytically and hence is accurate if the CFD simulation is accurate.
- Using a higher Reynolds number for a single geometry to see how the turbulent structures change and quantifying the increase in noise level.
- Checking for mesh independence and using a different mesh size for aeroacoustics and CFD to reduce size of data required to be exported.
- Using different turbulence models and comparing them to LES simulation.
- Using a more realistic vehicle geometry.

# Bibliography

- [1] W.R Stapleford and G.W Carr. Aerodynamic noise in road vehicles, part 1: The relationship between aerodynamic noise and the nature of airflow. The Motor Industry Research Association, 1971/2, November, 1970
- [2] W.R Stapleford. Aerodynamic noise in road vehicles, part 2: A study of the sources and significance of aerodynamic noise in saloon cars. The Motor Industry Research Association, 1972/6, November, 1970
- [3] J.R. Thomson. Wind noise- a practical approach. Society of Automotive Engineers, 840B, March 30- April 3, 1964.
- [4] T. Rung, E. Eschricht, J. Yan and F. Thiele. sound radiation of the vortex flow past a generic side mirror. 8<sup>th</sup> AIAA/CEAS Aeroacoustics Conference. Breckenridge, Colorado, AIAA-2002-2340, 17-19 June, 2002.
- [5] H. Posson and F. Perot. Far feild evaluation of the noise radiation by a side mirror using LES and acoustic analogy. 2<sup>nd</sup> AIAA/CEAS Aeroacoustics Conference. Cambridge, Massachusetts, AIAA-2006-2719, 8-10 May, 2006.
- [6] B.D Duncan, R Sengupta, S. Mallick, R Shock and D.B Sims-Williams. Numerical simulation and spectral analysis of pressure fluctuations in vehicle aerodynamic noise generation. Society of Automotive Engineering, 2002-01-0597, 2002.
- [7] J. D. Anderson. Modern Compressible Flow with historical perspective. New York: McGraw Hill, 3rd edition. ISBN 007-124136-1.
- [8] Leder, A. 1992 Abgelöste Strömungen Physikalische Grundlagen
- [9] A.R. George. Automobile aerodynamic noise. Society of Automotive Engineers, 900315, February 26 - March 2, 1990.
- [10] Lars Davidson. Fluid mechanics, turbulent flow and turbulence modeling. 2015.
- [11] H. Boden and M. Åbom. Modelling of fluid Machines as aources of sound in duct and pipe systems. Acta Acustica 3, 549-560, 1995.

- [12] S.W. Rienstra and A. Hirschberg. An introduction to acoustics. Report IWDE 01-03, Technische Universiteit Eindhoven, 2004.
- [13] D.C. Crighton. Basic principles of aerodynamic noise generation. *Prog. Aerospace Sci.*, 16:31-96, 1975.
- [14] H.K. Versteeg and W. Malalasekera. An introduction to computational fluid dynamics- the finite volume method. Harlow: Pearson Education ltd., 2 edition. ISBN 978-0-13-127498-3.
- [15] A.S. Lyrintzis. Integral acoustics method: From the (CFD) near-field to the (acoustic) far-field. *International Journal of Aeroacoustics* 2, 95-128, 2003.
- [16] M.J. Lighthill. On Sound Generated Aerodynamically. I. General Theory. *Proceedings of the Royal Society London, A* 211, 564-587, 1952.
- [17] M.J. Lighthill. On Sound Generated Aerodynamically. II. Turbulence as a source of sound. *Proceedings of the Royal Society London, A* 222, 1-34, 1954.
- [18] N. Curle. The influence of solid boundaries upon aerodynamic sound. *Proceedings of the Royal Society London, A* 231, 505-514, 1955.
- [19] M.E. Goldstein. *Aeroacoustics*. McGraw Hill book company, New York, 1976.
- [20] S.R. Ahmed and G. Ramm. Some salient features of the time averaged ground vehicle wake. SAE technical paper, 2004-01-1308, 2004.
- [21] T. Morel. Aerodynamic drag of bluff body shapes characteristic of Hatch-back cars. SAE paper 780267, 1978.
- [22] X. Nogueira, S. Khelladi, I. Colominas, L. Cueto-Felgueroso, J. París, and H. Gómez. High-resolution finite volume methods on unstructured grids for turbulence and aeroacoustics. *Archives of Computational Methods in Engineering*, 18(3):315-340, 2011.
- [23] Huadong Yao ; Lars Davidson ; Lars-Erik Eriksson ; Shia-Hui Peng ; O. Grundestam; P. E. Eliasson. Surface integral analogy approaches for predicting noise from 3D high-lift low-noise wings, *Acta Mechanica Sinica* (0567-7718). Vol. 30 (2014), 3, p. 326-338.

# A

## Appendix

### Matlab code for SPL and OASPL calculation

```
%% Postprocessing of Aeroacoustic data for three geometries Front to back
clear all
close all
clc

%% SPL calculation
dt = 0.001;    %time step
Fs = 1/dt;     %sampling frequency
P_ref = 0.00002; %reference pressure

load OBS_s_fb.dat %load data for three geometries
load OBS_n_fb.dat
load OBS_b_fb.dat

Ps = OBS_s_fb(:,2);
n = 11; % number of points specified
ls = length(Ps)/n;

Pss = reshape(Ps,[ls,n]);
ts = OBS_s_fb(1:ls,1); %time
Ls = length(Pss);
fs = Fs*(0:(Ls/2))/Ls; %frequency domain
Lfs = length(fs);
dfs = fs(2);

Pn = OBS_n_fb(:,2);
ln = length(Pn)/n;
Pnn = reshape(Pn,[ln,n]);
tn = OBS_n_fb(1:ln,1);
Ln = length(Pnn);
fn = Fs*(0:(Ln/2))/Ln;
Lfn = length(fn);
dfn = fn(2);
```

```

Pb = OBS_b_fb(:,2);
lb = length(Pb)/n;
Pbb = reshape(Pb,[lb,n]);
tb = OBS_b_fb(1:lb,1);
Lb = length(Pbb);
fb = Fs*(0:(Lb/2))/Lb;
Lfb = length(fb);
dfb = fb(2);

for i=1:n
Psmean(i) = mean(Pss(:,i));
Pnmean(i) = mean(Pnn(:,i));
Pbmean(i) = mean(Pbb(:,i));

Ps1 = Pss(:,i)-Psmean(i);
Pn1 = Pnn(:,i)-Pnmean(i);
Pb1 = Pbb(:,i)-Pbmean(i);

Ys = fft(Ps1);
Yn = fft(Pn1);
Yb = fft(Pb1);

Pyys = Ys.*conj(Ys);
Pyyn = Yn.*conj(Yn);
Pyyb = Yb.*conj(Yb);

splb= 10*log10(Pyys(1:(Lfs)))/(P_ref*P_ref); %SPL
spln= 10*log10(Pyyn(1:(Lfn)))/(P_ref*P_ref);
splb= 10*log10(Pyyb(1:(Lfb)))/(P_ref*P_ref);

figure(i) %plot SPL
semilogx(fs,spls,'LineWidth',1)
hold on
semilogx(fn,spln,'g','LineWidth',1)
semilogx(fb,splb,'r','LineWidth',1)
grid on
xlim([0 1000 ])
%title('Sound Pressure Level (SPL)')
xlabel('Frequency (Hz)')
ylabel('SPL')
legend('Slant','Notch','Square')

Is(i) = 2*dfs*sum(Pyys);
In(i) = 2*dfn*sum(Pyyn);

```

```
Ib(i) = 2*dfb*sum(Pyyb);
end

beta=0: pi/10 : pi;
OASPL_s = 10*log10(Is/(P_ref*P_ref)); %OASPL
OASPL_n = 10*log10(In/(P_ref*P_ref));
OASPL_b = 10*log10(Ib/(P_ref*P_ref));

figure(24)
polar(beta,OASPL_s,'*-')
hold on
polar(beta,OASPL_n,'g*-')
polar(beta,OASPL_b,'r*-')
grid on
%title('OASPL Front to Back')
%xlabel('Frequency (Hz)')
%ylabel('Pressure (Pa)')
legend('Slant','Notch','Square')
```